

DISSERTATION

IMAGING SINGLE BARIUM ATOMS IN SOLID XENON FOR BARIUM TAGGING IN THE  
NEXO NEUTRINOLESS DOUBLE BETA DECAY EXPERIMENT

Submitted by

Timothy Walton

Department of Physics

In partial fulfillment of the requirements

For the Degree of Doctor of Philosophy

Colorado State University

Fort Collins, Colorado

Fall 2015

Doctoral Committee:

Advisor: William M. Fairbank, Jr.

Bruce Berger  
Alan Van Orden  
Robert Wilson

Copyright by Timothy Walton 2015

All Rights Reserved

## ABSTRACT

The nEXO experiment will search for neutrinoless double beta decay of the isotope  $^{136}\text{Xe}$  in a ton-scale liquid Xe time projection chamber, in order to probe the Majorana nature of neutrinos. Detecting the daughter ( $^{136}\text{Ba}$ ) of double beta decay events, called barium tagging, is a technique under investigation which would provide a veto for a background-free measurement. This would involve detecting a single barium ion from within a macroscopic volume of liquid xenon. One proposed barium tagging method is to trap the barium ion in solid xenon (SXe) at the end of a cold probe, and then detect it by its fluorescence in the solid xenon. William M. Fairbank Jr.'s group at Colorado State University has been working toward this goal with steady success for some time. In this thesis, new studies on the spectroscopy of deposits of Ba and  $\text{Ba}^+$  in solid Xe are presented. Imaging of Ba atoms in solid Xe is demonstrated with ultimate sensitivity down to the single atom level.

## ACKNOWLEDGEMENTS

I thank my adviser William M. Fairbank, Jr. with inadequate words for his inspiring courage, foresight, and intuition as a physicist. The success of this thesis, those to come, and of the experimental method which they work toward belongs foremost to him. Special thanks also to Chris Chambers for tireless help with experiment and analysis, and ambition to continue the work. I thank him and Adam Craycraft for companionship and intellectual input. I thank Shon Cook and Brian Mong for developing the apparatus, pioneering the work, and training me along with Cesar Benitez and Kendy Hall. I also thank the nEXO collaboration for their support, and especially their spokesman Giorgio Gratta. I thank my wife for supporting and enduring the physicist lifestyle, and everyone in my family for inspiration and vital support.

This dissertation is typset in L<sup>A</sup>T<sub>E</sub>X using a document class designed by Leif Anderson.

Dedicated to my new son Logan.

## TABLE OF CONTENTS

Abstract .....	ii
Acknowledgements .....	iii
Chapter 1. Introduction .....	1
1.1. Neutrinos .....	2
1.2. Double Beta Decay .....	6
1.3. Enriched Xenon Observatory .....	8
Chapter 2. Theory .....	19
2.1. Ba/Ba <sup>+</sup> Spectroscopy in Vacuum .....	19
2.2. 5-level System .....	21
2.3. Matrix Isolation Spectroscopy .....	22
2.4. Fluorescence Efficiency .....	24
Chapter 3. Experimental .....	26
3.1. Ion Beam .....	26
3.2. Ba Getter Source .....	34
3.3. Sample Deposition .....	35
3.4. Laser Excitation .....	38
3.5. Collection Optics .....	41
3.6. Vibrations and Effective Laser Region .....	42
3.7. Laser Scanning .....	43
Chapter 4. Method .....	46
4.1. Wavelength Calibration .....	46

4.2. Fitting of Spectra .....	46
4.3. Optimizing Signal-to-Background .....	49
Chapter 5. Results: Spectroscopy .....	54
5.1. Excitation and Emission of Ba in SXe.....	54
5.2. 619-nm Peak Identification.....	57
5.3. Annealing/Temperature Dependence .....	58
5.4. Bleaching.....	62
5.5. Fluorescence Efficiency of 577- and 591-nm Peaks .....	68
5.6. Blue Excitation / Candidate Ba <sup>+</sup> Lines .....	68
Chapter 6. Results: Imaging .....	72
6.1. Imaging 577- and 591-nm peaks.....	73
6.2. Imaging 619-nm peak .....	76
6.3. Scanned Images.....	78
Chapter 7. Conclusions .....	81
7.1. Future Work.....	81
Bibliography .....	83

## CHAPTER 1

### INTRODUCTION

Neutrinos have been at the forefront of discovery in physics since their prediction by W. Pauli, who proposed in 1930 the existence of a neutral, unobserved particle to explain the apparent violation of energy conservation in beta decay [1]. He admitted that neutrinos (then deemed “neutrons” – what we now know as neutrons had not been discovered yet either) should be difficult to observe experimentally, but also that it seemed unlikely that they would never have been noticed before. As it turns out, they are much more difficult to observe than he predicted; they will not be noticed without extreme experimental techniques.

A theory formulated in 1933 by E. Fermi for beta decay [2], including the neutrino, would be the beginnings of weak interaction theory, and the development of the very successful Standard Model (SM) of particle physics. However, the SM assumes that neutrinos are massless. The discovery of non-zero neutrino mass via neutrino oscillations in the late 1990s [3] shows that there is more new physics to be discovered, and presents a path to follow.

Neutrinos are difficult to study, but the rewards are profound. The See-saw Mechanism is a theory which predicts the extreme lightness of neutrinos, while also predicting very heavy neutrino partners. The existence of heavy neutrinos in the high-energy environment of the early universe, coupled with the possibility of the violation of CP conservation which could slightly favor the production of matter vs. anti-matter in decays of these heavy neutrinos, could explain why the universe became dominated by matter. [4]

If this theory is correct, then neutrinos would be described by the Majorana formulation rather than Dirac, and the process of neutrinoless double beta decay ( $0\nu\beta\beta$ ) would be allowed. Observation of  $0\nu\beta\beta$  would simultaneously demonstrate that neutrinos are Majorana

particles, as well as aid in determining the absolute mass itself [5]. This chapter outlines the current theory for neutrinos, and then describes the  $0\nu\beta\beta$  experiments EXO-200 and nEXO, in order to motivate barium tagging for nEXO.

## 1.1. NEUTRINOS

Neutrinos are chargeless leptons which only interact via the weak force (and gravity). There are three known “flavors” of neutrinos,  $\nu_e$ ,  $\nu_\mu$ , and  $\nu_\tau$ , each corresponding to one of the three known leptons. These are the eigenstates in the basis of the weak force, so they are the states in which a neutrino will interact via the weak force.

### 1.1.1. NEUTRINO OSCILLATION AND MASS

The postulate that neutrinos have an energy basis which is different from the flavor basis predicts the phenomenon of oscillation – that the time evolution of an initially pure flavor state (as a neutrino will be produced) will result in a time-dependent probability of measuring the other two flavors as well.

The very small mass of a neutrino (assumed zero in the SM), specifically relative to its momentum, lets one write its Hamiltonian in terms of mass squared differences  $\Delta m_{ij}^2 = m_i^2 - m_j^2$ , where  $i,j = 1,2,3$ , referring to what we then call mass states. The mass basis is really the energy basis with the small mass approximation, along with dropping some constant terms in the Hamiltonian (which do not affect time evolution).

The mixing between the 3-vector mass and flavor bases is defined by a rotation in terms of three mixing angles,  $\theta_{12}$ ,  $\theta_{23}$ , and  $\theta_{13}$ . Transformation between the flavor and mass bases is done with the following unitary matrix, called the Pontecorvo–Maki–Nakagawa–Sakata (PMNS) matrix [6]:

$$\begin{aligned}
(1) \quad U &= \begin{pmatrix} 1 & 0 & 0 \\ 0 & c_{23} & s_{23} \\ 0 & -s_{23} & c_{23} \end{pmatrix} \begin{pmatrix} c_{13} & 0 & s_{13}e^{-i\delta} \\ 0 & 1 & 0 \\ -s_{13}e^{i\delta} & 0 & c_{13} \end{pmatrix} \begin{pmatrix} c_{12} & s_{12} & 0 \\ -s_{12} & c_{12} & 0 \\ 0 & 0 & 1 \end{pmatrix} \begin{pmatrix} 1 & 0 & 0 \\ 0 & e^{i\alpha_1/2} & 0 \\ 0 & 0 & e^{i\alpha_2/2} \end{pmatrix} \\
&= \begin{pmatrix} c_{12}c_{13} & s_{12}c_{13} & s_{13}e^{-i\delta} \\ -s_{12}c_{23} - c_{12}s_{23}s_{13}e^{i\delta} & c_{12}c_{23} - s_{12}s_{23}s_{13}e^{i\delta} & s_{23}c_{13} \\ s_{12}s_{23} - c_{12}c_{23}s_{13}e^{i\delta} & -c_{12}s_{23} - s_{12}c_{23}s_{13}e^{i\delta} & c_{23}c_{13} \end{pmatrix} \begin{pmatrix} 1 & 0 & 0 \\ 0 & e^{i\alpha_1/2} & 0 \\ 0 & 0 & e^{i\alpha_2/2} \end{pmatrix}
\end{aligned}$$

where  $c_{ij} = \cos \theta_{ij}$  and  $s_{ij} = \sin \theta_{ij}$ .  $\delta$  and  $\alpha_i$  are Dirac and Majorana, respectively, CP-violating phases. Transformation between bases is done by Eqn. 2:

$$\begin{aligned}
(2) \quad |\nu_\alpha\rangle &= \sum_i U_{\alpha i}^* |\nu_i\rangle, \\
|\nu_i\rangle &= \sum_\alpha U_{\alpha i} |\nu_\alpha\rangle.
\end{aligned}$$

A two-neutrino approximation demonstrates how this results in neutrino oscillation. In this case, there is only one mixing angle  $\theta$  and one mass squared difference  $\Delta$ , and the Hamiltonian  $H$  and mixing matrix  $U$  are as follows:

$$\begin{aligned}
(3) \quad H &= \frac{1}{4E} \begin{pmatrix} -\Delta & 0 \\ 0 & \Delta \end{pmatrix} \\
U &= \begin{pmatrix} \cos \theta & \sin \theta \\ -\sin \theta & \cos \theta \end{pmatrix}.
\end{aligned}$$

Applying time evolution to, say, a pure electron neutrino (where the two neutrino flavors here are  $\nu_e$  and  $\nu_\mu$ ) then leads to the following state:

$$(4) \quad \begin{aligned} |\nu_e(t)\rangle &= (e^{it\Delta/4E} \cos^2 \theta + e^{-it\Delta/4E} \sin^2 \theta) |\nu_e(0)\rangle \\ &\quad + \cos \theta \sin \theta (-e^{it\Delta/4E} + e^{-it\Delta/4E}) |\nu_\mu(0)\rangle \end{aligned}$$

where  $E$  is the neutrino energy. Note that if  $\theta$  is zero, the case where the mass basis is the same as the flavor basis, the state remains pure  $\nu_e$ . The same is true if  $\Delta$  is zero. Thus, the discovery of neutrino oscillation, i.e. the discovery of mixed amplitudes in propagation equations like Eqn. 4, was the first (and only, so far) demonstration that neutrinos have a non-zero mass (*particularly a non-zero mass squared difference*).

Studying oscillations of neutrinos from different kinds of sources, with different energies and path lengths, can isolate sensitivities to the different mixing angles and mass squared differences. For example, the study of solar neutrinos (neutrinos emanating from nuclear fusion reactions in the core of the sun) provides sensitivity to  $\theta_{12}$  and  $\Delta m_{12}^2$ . The oscillation parameters so far measured are shown in Table 1.1.

TABLE 1.1. Best-fit values for neutrino oscillation parameters, from a global fit to oscillation experiment data. Parameters which depend on the mass hierarchy have values for NH (IH). The atmospheric parameter  $\Delta m^2$  is defined as  $\Delta m^2 = \Delta m_{31}^2 - \Delta m_{21}^2/2 > 0$  ( $\Delta m^2 = \Delta m_{32}^2 + \Delta m_{21}^2/2 < 0$ ). [6]

Parameter	Measurement ( $\pm 1\sigma$ )
$\Delta m_{12}^2$	$7.54_{-0.22}^{+0.26} 10^{-5} \text{ eV}^2$
$ \Delta m^2 $	$2.43 \pm 0.06 (2.38 \pm 0.06) 10^{-3} \text{ eV}^2$
$\sin^2 \theta_{12}$	$0.308 \pm 0.017$
$\sin^2 \theta_{23}$	$4.37_{-0.023}^{+0.033} (4.55_{-0.031}^{+0.039})$
$\sin^2 \theta_{13}$	$0.0234_{-0.0019}^{+0.0020} (0.0240_{-0.0022}^{+0.0019})$
$\delta/\pi$ ( $2\sigma$ range)	$1.39_{-0.27}^{+0.38} (1.31_{-0.33}^{+0.29})$



FIGURE 1.1. The two possible hierarchies of neutrino masses. The colors depict the mixing between the mass and flavor bases.

Note that only the absolute value of the atmospheric neutrino oscillation parameter  $\Delta m^2$  is known. As a consequence, there are two possibilities for the hierarchy of the three neutrino masses. These are called the Normal and Inverted Hierarchies, as shown in Fig. 1.1. The correct mass hierarchy remains unknown, but next-generation neutrino experiments, possibly including nEXO, may be able to discern this.

Neutrino oscillation demonstrates that neutrinos have non-zero mass, and though oscillation experiments measure the mass squared differences, the absolute masses of the three neutrinos remain unknown. Cosmology can put limits on the sum of the three neutrino masses. The Planck collaboration reports an upper bound on this sum at  $\sum_i m_i < 0.23 \text{ eV}$  [7]. The KATRIN experiment will search for absolute neutrino mass with sensitivity of  $m_{\bar{\nu}_e} < 0.2 \text{ eV}$  (90% CL) by measuring the spectrum of tritium beta decay near the Q-value (maximal decay energy) [8].



FIGURE 1.2. Two-neutrino (left) and neutrinoless (right) double beta decay.

## 1.2. DOUBLE BETA DECAY

Double beta decay is the simultaneous decay of two neutrons in a nucleus into two protons and two electrons. Two-neutrino double beta decay ( $2\nu\beta\beta$ ), shown in Fig. 1.2(left), is allowed by the Standard Model and has been observed in eleven isotopes with half-lives between  $10^{19}$  and  $10^{21}$  years. Similar to beta decay, a neutrino accompanies each electron in this decay, broadening the spectrum of the summed electron energy. This is a second-order process, making it a rare decay, and requiring low backgrounds to measure.

$0\nu\beta\beta$ , shown in Fig. 1.2(right), is a postulated mode of double beta decay. In this case, the neutrino is exchanged as a virtual particle (which would require that it is a Majorana particle), and there are no neutrinos in the final products. If discovered, not only would neutrinos be determined to be Majorana particles, but the measured  $0\nu\beta\beta$  half-life would also aid in determining absolute neutrino mass according to Eqn. 5:

$$(5) \quad T_{1/2}^{0\nu} = (G^{0\nu}(Q, Z)|M^{0\nu}|^2 \langle m_\nu \rangle^2)^{-1}$$



FIGURE 1.3. Conceptual two-neutrino (blue) and zero-neutrino (red) double beta decay spectra.

where  $T_{1/2}^{0\nu}$  is the  $0\nu\beta\beta$  half-life,  $G^{0\nu}$  is a known phase space factor, and  $M^{0\nu}$  is a model-dependent nuclear matrix element.  $\langle m_\nu \rangle$  is the effective Majorana neutrino mass:

$$(6) \quad \langle m_\nu \rangle = \sum_i U_{ei}^2 m_i.$$

The sum of the energies of the emitted electrons in double beta decay will serve as the distinction between the two-neutrino and zero-neutrino modes, shown in Fig. 1.3. In the two-neutrino mode, the total decay energy is shared probabilistically between the electrons and the neutrinos (the nuclear recoil energy is negligible), resulting in a broad distribution in the summed electron energy. (Recall the similarly broad electron energy in single beta decay, which ultimately led to discovery of the neutrino involved.) But in the zero-neutrino mode, essentially all of the decay energy is carried away by the two electrons, resulting in only a single allowed value for the summed electron energy – a peak in the summed electron energy spectrum at the Q-value.

The rarity of double beta decay requires very low backgrounds, especially around the Q-value for the  $0\nu\beta\beta$  search. The next sections describe the experiments EXO-200 and its next-generation successor, nEXO.

### 1.3. ENRICHED XENON OBSERVATORY

EXO-200 and nEXO (EXO standing for Enriched Xenon Observatory) are a progression of two experiments, each a liquid xenon (LXe) time projection chamber (TPC) designed to study the double beta decay of the isotope  $^{136}\text{Xe}$ , and ultimately to search for the zero-neutrino mode.  $^{136}\text{Xe}$  is fairly unique among the double beta decay isotopes in that it can be studied in a gas or liquid TPC instead of solid crystals or foils. The 3D event position reconstruction abilities of a TPC have advantages in background reduction, described in section 1.3.1. Purification of Xe is straightforward and can be done continuously in a detector. LXe is transparent, and produces substantial ionization and scintillation at 178 nm when energy is deposited in the LXe [9]. A liquid TPC approach also offers the opportunity to identify, or “tag”, the daughter  $^{136}\text{Ba}^{++}$  at the site of the double beta decay event, which would provide a method for background-free identification of  $0\nu\beta\beta$  [10]. Barium tagging is the focus of our group at CSU and is the subject of this thesis. The following sections describe the EXO-200 experiment, as well as nEXO, the next-generation tonne-scale LXe TPC, which is now in the research and development stage. EXO-200 does not have barium tagging implemented, but it is hoped that nEXO will.

#### 1.3.1. EXO-200

Located about half a mile underground in the Waste Isolation Pilot Plant (WIPP) near Carlsbad, NM, EXO-200 has been operational since 2011. It is a TPC using LXe enriched



FIGURE 1.4. Drawing of EXO-200 TPC Vessel with surrounding cryostat, lead walls, and muon veto panels.

to  $80.672\% \pm 0.14\%$   $^{136}\text{Xe}$  [9], with a fiducial volume corresponding to 66.20 kg of  $^{136}\text{Xe}$ .

It is designed to probe Majorana neutrino masses down to around 109-135 meV (the range covers different matrix element calculations) [11]. The WIPP mine is in a salt basin, which contains lower levels of Uranium and Thorium than rock in a typical mine.

A schematic diagram of the TPC in the class 100 cleanroom is shown in Fig. 1.4. Several layers of lead wall surround the copper cryostat, which is filled with HFE-7000, a cryogenic fluid which keeps the TPC cooled to LXe temperatures, as well as aids in shielding the detector. The TPC vessel is made of low-radioactivity copper, and is kept as thin as possible to minimize backgrounds. Scintillating panels on the outside of the cleanroom provide a cosmic ray muon veto.



FIGURE 1.5. EXO-200 TPC cutaway view [9].

A cut-away view of the EXO-200 detector is shown in Fig. 1.5. It is two mirrored TPCs which share a cathode. The detection planes are a combination of ionized charge induction/collection wires and large area avalanche photodiodes (LAAPDs), which detect scintillation light [12].

A view into one of the TPCs is shown in Fig. 1.6. On the detection plane, holes for the LAAPDs can be seen below the cross-hatched u- and v-wires. The white material on the inner wall is the Teflon reflector. When a double beta decay event occurs in the LXe,

the energetic electrons ionize many surrounding Xe atoms, as well as produce a scintillation signal. Scintillation light provides an initial time for z-measurement of the event, as well as an energy measurement.

The cathode is set to -8 kV, providing an electric field of 374 V/cm across the 20 cm drift length of each TPC. Ionized electrons drift from the decay site, first passing the v-wires, which receive an induction signal, and are then collected by the u-wires, which are set at a 60° angle from the v-wires, as depicted in Fig. 1.7. An electric field of 778 V/cm between the u- and v-wires ensures 100% v-wire transparency. The charge collection provides an energy measurement complimentary to that of the scintillation. Together, the u- and v-wires give an x/y position measurement for the event. The time between the initial scintillation detection and the charge collection give a z position. Thus a 3D position can be reconstructed for the event if u-wire, v-wire, and scintillation signals are detected. [9]

Having a reconstructed 3D event position is important in several ways. Firstly, position-based corrections to scintillation and charge collection can be applied. For charge, electronegative impurities in the LXe will absorb the drifting charge, requiring a drift-length (z-position) correction. High purity levels, measured in terms of electron lifetime, of  $2\text{--}3 \times 10^3$   $\mu\text{s}$  and higher are maintained in EXO-200, resulting in a small correction of a few % for maximal drift lengths. For scintillation, a 3D correction is applied, as some regions have more efficient light collection by the LAAPDs. A 3D position also allows a fiducial volume to be defined. A standoff distance from detector surfaces aids in distinction between gamma ray events and double beta decay events, as gamma interactions tend to occur on detector materials, while double beta decay are uniformly distributed in the LXe. Gamma



FIGURE 1.6. View of the detection plane in one of the two EXO-200 TPCs.



FIGURE 1.7. EXO-200 event topology.

rays also exhibit some attenuation in the LXe. Finally, 3D reconstruction allows the distinction between single-site (SS) and multi-site (MS) events. A MS event is one where two spatially separated events occur in the same  $2048\text{-}\mu\text{s}$  time window. These are mostly caused by gamma events, which can Compton-scatter several times in the LXe. Rejecting MS events further aids in separating gamma events from double beta decay events. [9] Barium tagging will also benefit from a 3D reconstructed position in nEXO.

The final data set is fit using a combination of probability distribution functions (PDFs) for  $0\nu\beta\beta$ ,  $2\nu\beta\beta$ , and background components. Fits to the final energy spectrum data for (a) SS events, and (b) MS events are shown in Fig. 1.8 for the most recent  $0\nu\beta\beta$  analysis. The green bands beneath each plot show the residuals vs. energy. The  $2\nu\beta\beta$  spectrum, in gray, dominates the signal in the SS spectrum below the Q-value. The vertical red lines in the SS spectrum outline the  $\pm 2\sigma$  region of interest around the Q-value, where the  $0\nu\beta\beta$  peak will lie. The insets are a zoom into this region. The fit value for  $0\nu\beta\beta$  in this dataset is non-zero, but it is consistent with the null hypothesis at  $1.2\sigma$ . This sets an upper limit on the  $0\nu\beta\beta$  half-life at  $T_{1/2}^{0\nu\beta\beta} < 1.1 \times 10^{25}$  yr (90% CL), which corresponds to  $\langle m_{\nu_e} \rangle < 190\text{-}450$  meV depending on nuclear matrix element calculations [14]. EXO-200 reports the  $2\nu\beta\beta$  half-life measurement in [9] of  $T_{1/2}^{2\nu\beta\beta} = 2.165 \pm 0.016(\text{stat}) \pm 0.059(\text{sys}) \times 10^{21}$  yr. This is more precise but consistent with previous measurements by EXO-200 in 2011 [15] and KamLAND-ZEN in 2012 [16].

### 1.3.2. nEXO

The next-generation successor to EXO-200 is nEXO, a tonne-scale LXe TPC which will probe Majorana neutrino masses down to the 10 meV scale. The sensitivity projections for nEXO are shown in Fig. 1.9, along with those of EXO-200. nEXO will reach phase space



FIGURE 1.8. EXO-200 energy spectrum from  $0\nu\beta\beta$  search analysis [14].

where the two possible mass hierarchies split, and will probe the full phase space of the inverted hierarchy. Barium tagging will push the sensitivity further into the region allowed only by the normal hierarchy.

A schematic diagram of the nEXO in the SNOLAB cryopit, one of the possible locations for nEXO, is shown in Fig. 1.10. Similar to EXO-200, the copper-housed TPC will be submerged in HFE fluid, inside a copper cryostat. The cryostat will be insulated and submerged in a large volume of water shielding, in which photo-multiplier tubes could provide muon veto by observing Cherenkov radiation. nEXO will be a single TPC with charge and light



FIGURE 1.9. nEXO projected sensitivity to the Majorana neutrino mass vs. the minimum of the three masses  $m_{min}$ . Solid (dotted) lines are  $1(2)$ - $\sigma$  bands on measured neutrino oscillation parameters. [can I have this in here?](#)

readouts at opposing ends of the TPC. Rather than wires, nEXO will use tile electrodes for charge readout, shown in Fig. 1.11. Silicon photo-multipliers will be used for light detection.

### 1.3.3. BARIUM TAGGING

The ability to observe the daughter of each  $0\nu\beta\beta$  event is the ultimate background rejection technique. Several possible barium tagging techniques have been proposed for nEXO. The original and most natural concept is to direct one or more lasers at the decay



FIGURE 1.10. nEXO TPC in the SNOLAB cryopit.



FIGURE 1.11. nEXO readout.

site to induce fluorescence of the barium daughter [10]. This technique was explored by the Fairbank group, and was abandoned when  $\text{Ba}^+$  fluorescence could not be confidently observed in LXe [17].

A few barium tagging techniques continue to be explored. One of these is to grab the daughter on a probe surface, brought to the decay site by a probe. It would then be moved to a location where it can be desorbed from that surface by an infrared laser, and subsequently resonantly ionized by two lasers in order to detect it by time-of-flight spectroscopy. The apparatus for the study of this method is described in [18], along with some initial results.

The other remaining technique for barium tagging, now the focus of the Fairbank group and the subject of this thesis, is called tagging in SXe. Here, a cold probe would go to the site of the candidate  $0\nu\beta\beta$  event in order to trap the  $\text{Ba}/\text{Ba}^+$  in a small amount of SXe, and then observe it by its laser-induced fluorescence in the SXe, a technique called matrix isolation spectroscopy. A concept for a probe is shown in Fig. 1.12. The SXe forms on a sapphire window at the end of the probe. Sapphire is a good candidate for a substrate because it has good thermal conductivity at low temperature and is highly transparent. An excitation laser would be brought into the probe through a fiber, and aimed through the sapphire to excite the  $\text{Ba}/\text{Ba}^+$  in the SXe. A return fiber could collect the laser reflections to measure the SXe thickness via interference fringes. The  $\text{Ba}/\text{Ba}^+$  fluorescence would then be collected by a lens/filter system and imaged onto a CCD. Additional components, not shown, would be required for cooling the sapphire, either by liquid He or by a Joule-Thompson nozzle, as well as a thermometer.

Whether the daughter Ba will neutralize or remain ionized is not yet known. It is however expected that a  $\text{Ba}^{++}$  ion will neutralize at once to  $\text{Ba}^+$  by charge transfer in LXe, since the



FIGURE 1.12. Concept for a cryoprobe containing excitation/collection optics.

LXe conduction band gap is slightly less than the ionization potential for  $\text{Ba}^+$  [10]. Further neutralization by recombination with the electron cloud could also occur. However, a study of neutralization of beta decay daughters in EXO-200 has observed a high percentage, 76(5)%<sup>1</sup>, of ionized daughters [ref alphaion]. This provides some expectation of a high percentage of ionized  $0\nu\beta\beta$  daughters.

## CHAPTER 2

### THEORY

#### 2.1. BA/BA<sup>+</sup> SPECTROSCOPY IN VACUUM

Transition rates for the lowest-lying energy levels in vacuum are shown in Table 2.1 for Ba and Ba<sup>+</sup>. For Ba, the main transition is between the ground  $6s^2 \ ^1S_0$  to the excited  $6s6p \ ^1P_1^o$ , however branching ratios from the P state result in a decay to one of three metastable D states in about 1 in 330 excitations. For Ba<sup>+</sup>, two strong transitions exist between the ground  $6s \ ^2S_{1/2}$  and the  $6p \ ^2P_{1/2}$  and  $6p \ ^2P_{3/2}$  excited states. Transitions to the two metastable D states are higher than for the atom, resulting in a decay into a D state after about 4 excitations. These D states are metastable because they are parity-forbidden to decay back to the ground state, resulting in much lower decay rates.

TABLE 2.1. *the 5-s one is 8 s for measurement in [11] of phys rev a 46 5 (1992), is 1/lifetime is right.*

	Transition	Rate ( $s^{-1}$ )	Ref.
Ba	$6s6p \ ^1P_1^o \rightarrow 6s^2 \ ^1S_0$	$1.19 \times 10^8$	[21]
	$6s6p \ ^1P_1^o \rightarrow 6s5d \ ^1D_2$	$2.50 \times 10^5$	[21]
	$6s6p \ ^1P_1^o \rightarrow 6s5d \ ^3D_2$	$1.1 \times 10^5$	[21]
	$6s6p \ ^1P_1^o \rightarrow 6s5d \ ^3D_1$	$3.1 \times 10^3$	[21]
	$6s5d \ ^1D_2 \rightarrow 6s^2 \ ^1S_0$	5	[?]
	$6s5d \ ^3D_2 \rightarrow 6s^2 \ ^1S_0$	$1.4^{-2}$	[?]
	$6s5d \ ^3D_1 \rightarrow 6s^2 \ ^1S_0$	$1.7^{-2}$	[?]
Ba <sup>+</sup>	$6p \ ^2P_{3/2}^o \rightarrow 6s \ ^2S_{1/2}$	$1.11 \times 10^8$	[21]
	$6p \ ^2P_{1/2}^o \rightarrow 6s \ ^2S_{1/2}$	$9.53 \times 10^7$	[21]
	$6p \ ^2P_{3/2}^o \rightarrow 5d \ ^2D_{5/2}$	$4.12 \times 10^7$	[21]
	$6p \ ^2P_{3/2}^o \rightarrow 5d \ ^2D_{3/2}$	$6.00 \times 10^6$	[21]
	$6p \ ^2P_{1/2}^o \rightarrow 5d \ ^2D_{3/2}$	$3.10 \times 10^7$	[21]
	$5d \ ^2D_{5/2} \rightarrow 6s \ ^2S_{1/2}$	$3.8 \times 10^{-2}$	[22]
	$5d \ ^2D_{3/2} \rightarrow 6s \ ^2S_{1/2}$	$1.3 \times 10^{-2}$	[23]

Single atom/ion detection by spectroscopy generally requires, in addition to the main excitation laser, lasers to provide transitions out of the metastable D states once the atom/ion



FIGURE 2.1. Ba energy levels in vacuum.

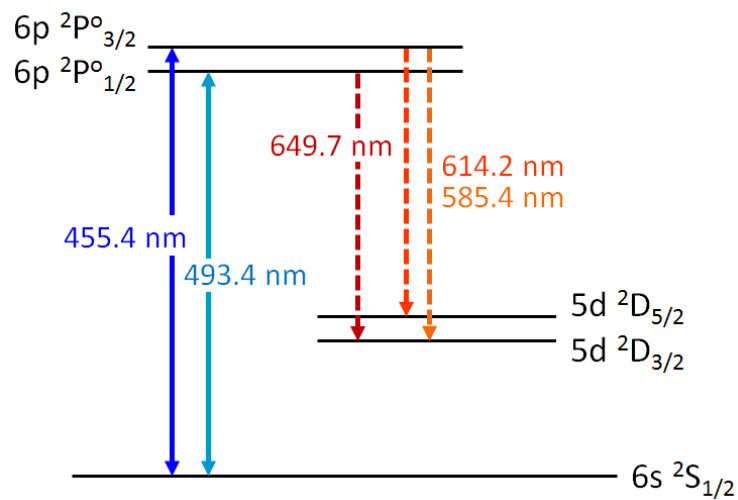


FIGURE 2.2.  $Ba^+$  energy levels in vacuum.

decays into one of them. For the atom, for which some of the lowest-lying energy levels are shown in Fig. 2.1, re-pumping can be accomplished via three additional infrared lasers for the direct transitions back to the  $6s6p\ ^1P_1^o$  state, and also via excitation to higher-level states which have paths back into the fluorescence cycle. A few such higher-level re-pump transitions are shown in Fig. 2.1, including two red transitions to the  $5d6p\ ^3D_1^o$ , and blue and violet transitions to the  $6s7p\ ^1P_1^o$  and  $6s8p\ ^1P_1^o$  states. Trapping/detection of Ba atoms in a magneto-optical trap (MOT) was achieved in [24] with all three infrared re-pump transitions, as well as with *look up the other one*. Observation of trapped single Ba<sup>+</sup> ions requires only two lasers if the  $^2P_{1/2}$  excited state is used, e.g. [25].

## 2.2. 5-LEVEL SYSTEM

A solution to the 5-level rate equation for atomic Ba transitions, utilized in Sec. 5.4.1 for comparison with bleaching data, was done numerically. The rate equation is stated in Eqn. 7:

$$(7) \quad \begin{aligned} \frac{dN_1}{dt} &= -W_{12}N_1 + A_{21}N_2 + A_{31}N_3 + A_{41}N_4 + A_{51}N_5 \\ \frac{dN_2}{dt} &= W_{12}N_1 - N_2(A_{21} + A_{23} + A_{24} + A_{25}) \\ \frac{dN_3}{dt} &= A_{23}N_2 - A_{31}N_3 \\ \frac{dN_4}{dt} &= A_{24}N_2 - A_{41}N_4 \\ \frac{dN_5}{dt} &= A_{25}N_2 - A_{51}N_5 \end{aligned}$$

where  $N_i$  is the population in state  $i$ ,  $A_{ij}$  is the decay rate from state  $i$  to state  $j$ , and  $W_{12}$  *check italicization of w12 elsewhere* is the excitation rate. States 1 and 2 represent the

ground and excited states, respectively, and states 3, 4 and 5 represent the ??? metastable states, respectively.

### 2.3. MATRIX ISOLATION SPECTROSCOPY

In the matrix isolation spectroscopy technique [26], a species of interest is embedded and trapped in an inert host matrix, e.g. a solid noble gas. Low concentrations of the guest species, ideally at least 1:10<sup>3</sup> host:guest ratio, prevent guest-guest interactions.

The proposed method of Ba tagging in SXe is a unique application of the matrix isolation spectroscopy technique. It is important to understand the effects we might expect from the interaction between the guest Ba/Ba<sup>+</sup> and the host Xe atoms. The ground S state of Ba, as well as for Ba<sup>+</sup>, is spherically symmetric, and being slightly larger in Van der Waals radius than Xe, it is likely to take the place of one or more Xe atoms in the fcc crystal (substitution), vs. existing in between Xe atoms in the crystal structure (interstitial). However, the strength of the Ba-Xe interaction, an induced dipole-dipole Van der Waals force, is quite different when the Ba is in the non-spherically-symmetric excited P state [27]. This leads to significant broadening of absorption and emission for the Ba, as well as an energy shift between the two, according to the Franck Condon Principle, illustrated in Fig. 2.3. In a cold matrix, the system will be in the ground lattice vibrational state ( $\nu = 0$ ) before excitation. Electronic excitation can occur to multiple vibrational modes whose wavefunctions overlap that of the ground state, thus broadening the absorption energy. In the excited state, rapid decay occurs to the lowest vibrational mode, and then a similar broadening in the spontaneous emission energy occurs. A redshift in the emission is observed relative to the excitation.

As as example *is there a more modern example paper you can use?*, the spectroscopy of Ba in solid Ar (SAr) and solid Kr (SKr) matrices was studied in [28]. The example of Ba in

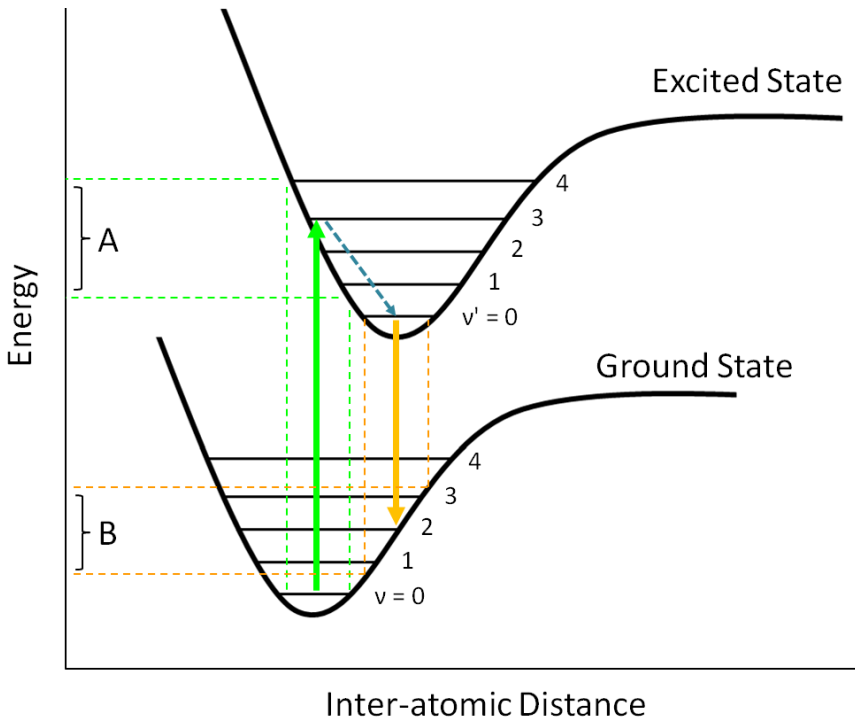


FIGURE 2.3. Illustration of the Franck-Condon Principle resulting in red-shifted emission as well as broadening in absorption (A) and emission (B) due to vibrational modes  $\nu$  ( $\nu'$ ) in the ground (excited) state.

SAr is shown in Fig. 2.4. The absorption is 10s of nm broad with a multi-peak structure, and the emission is broadened to nms and red-shifted. These were attributed to the main  $6s^2$   ${}^1S_0 \rightarrow 6s6p {}^1P_1^o$  transition and its spontaneous emission. *talk about other aspects....brian says the triplet is caused by P state degeneracy being split, but I don't see how this makes sense, and also I have the impression that there are multiple explanations like Jahn Teller – you should have a feel for this....*

Energy level transition probabilities can also be affected in a matrix, e.g., spin-forbidden transitions can become more significant via the heavy atom effect [ref...i know you have crepin but maybe you can use crepin's ref, since you need to understand this anyway]. If electronic potential energy curves cross each other, non-radiative transitions can become allowed for otherwise forbidden transitions. [27] Effects like these could aid in observation of

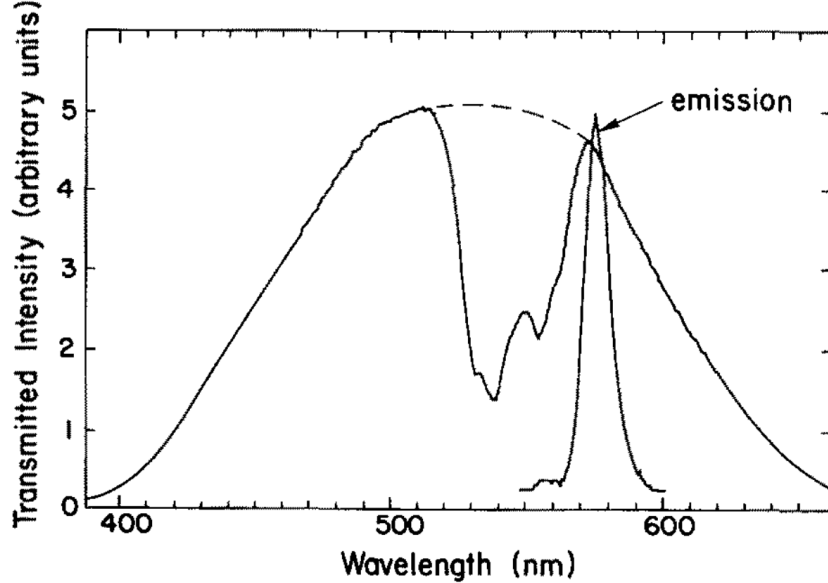


FIGURE 2.4. Absorption and emission spectra of neutral Ba in SAr at 10 K. [28]

the Ba/Ba<sup>+</sup>, e.g. by improving decay rates out of metastable D states, or they could reduce detectability, e.g. if a non-radiative decay competes with the fluorescence channel.

#### 2.4. FLUORESCENCE EFFICIENCY

Fluorescence efficiency ( $\epsilon_f$ ) is the ratio of fluorescence photons emitted to excitations into the fluorescing state. This becomes less than one when there are paths out of the excited state other than the one which emits the photon being measured, e.g. the  $\epsilon_f$  of Ba in vacuum is about 99.7%, not quite 1 due to about 1 in 330 decays from the P state into a metastable D.  $\epsilon_f$  can be calculated by Eqn. 8:

$$(8) \quad \epsilon_f = \frac{f}{w_{12}\epsilon_c} = \frac{fh\nu}{\sigma I \epsilon_c}$$

where  $f$  is the number of fluorescence photons observed per atom per second,  $w_{12}$  is the excitation rate,  $\epsilon_c$  is the collection efficiency of the system,  $\sigma$  is the cross section for the excitation interaction,  $I$  is the laser intensity, and  $h\nu$  is the excitation photon energy.

## CHAPTER 3

# EXPERIMENTAL

This chapter describes the apparatus at Colorado State University which was used for producing and observing deposits of Ba/Ba<sup>+</sup> in SXe. The main barium source, a Ba<sup>+</sup> ion beam, is first described, as well as a neutral Ba getter source. The co-deposit of Ba/Ba<sup>+</sup> with Xe gas onto a cold sapphire window, subsequent laser excitation, and finally the collection optics for the fluorescence are described.

### 3.1. ION BEAM

The ion beam system is shown in Fig. 3.1. This is a clean source of Ba<sup>+</sup> which can do a very wide range of deposit sizes, from billions of ions in a focused laser region all the way down to the single-ion level and below.

#### 3.1.1. ION SOURCE

Ba<sup>+</sup> ions are produced in a Model DCIS-101 Colutron ion gun system [29]. The source is shown in Fig. 3.2. A solid barium charge is placed into the hollowed end of a stainless steel rod, which is inserted into the discharge chamber, where it is heated by a filament. The barium vaporizes, and escapes the hollowed rod around a loosely threaded set screw. The source is designed to produce a discharge between the anode plate and the filament cathode, through an argon buffer gas leaked into the source chamber. This controlled discharge would then also ionize atoms from the solid charge to produce the desired ion beam, and Ar ions would be filtered out. However, to avoid contamination of the SXe matrix with residual Ar gas, the buffer gas was not used in this work. Discharge can be maintained with Ba vapor alone. The longevity of ion current from a single charge (at least several 10s of hours)

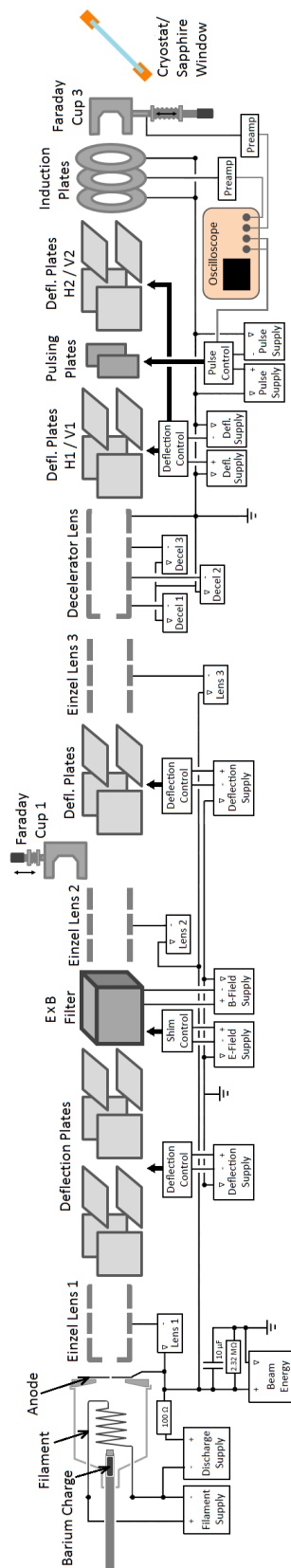


FIGURE 3.1.  $\text{Ba}^+$  ion beam.

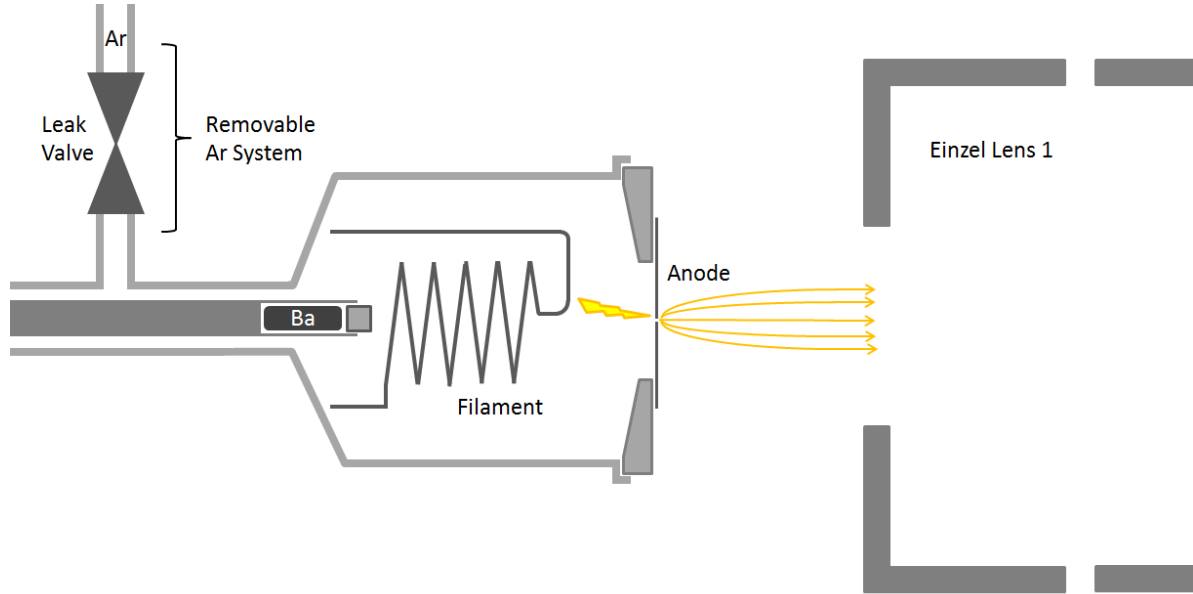


FIGURE 3.2.  $\text{Ba}^+$ / $\text{Ar}^+$  ion source.

suggests that Ba is coating the inner walls of the source chamber, and is heated enough to provide sufficient Ba pressure to support a discharge. The discharge produces a plasma, containing barium ions, which escapes the chamber through a small hole in the anode, where it enters the acceleration region. The acceleration potential applied is 2 kV, between the ion source anode and the first element of Einzel lens 1 (L1). This lens approximately collimates the ion beam for passage through the  $E \times B$  velocity filter.

### 3.1.2. $E \times B$ VELOCITY FILTER

The  $E \times B$  velocity filter selects  $\text{Ba}^+$  by creating perpendicular electric and magnetic fields, which produce opposing forces on charged particles moving through the filter. The opposing forces will be equal for ions with velocity  $v = \frac{E}{B}$ . Since ion velocity is determined by mass ( $m$ ), charge ( $q$ ) and beam potential ( $V$ ), the filter selects ions satisfying Eqn. 9:

$$(9) \quad \frac{m}{q} = \frac{2VB^2}{E^2}$$

where  $B$  and  $E$  are the magnetic and electric fields, respectively. Those fields are chosen such that  $\text{Ba}^+$  ions pass straight through. Other ions will be deflected.

The  $E \times B$  filter is shown in Fig. 3.3. Electromagnets provide the vertical magnetic field. Electrode plates and field-shaping guard rings provide the horizontal electric field. The guard rings prevent a lensing and astigmatism effect from fringe fields of the plates [29].

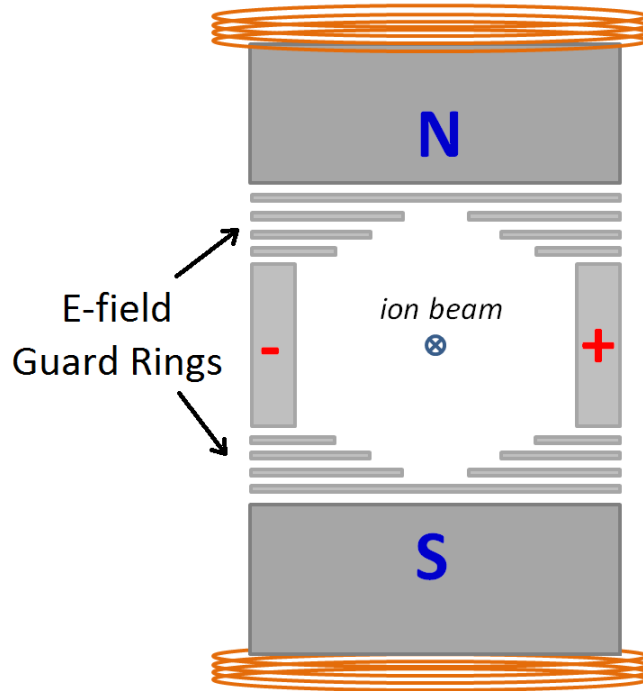


FIGURE 3.3. Colutron  $E \times B$  ion velocity filter.

### 3.1.3. OTHER BEAM COMPONENTS

The first three sets of deflection plates can be used for beam diagnostics, and are set to 0 V during normal operation. The deflection plates just before the pulsing plates, H1 and

V1, are set to constant values of +50 V and 0 V, respectively, which have been selected such that the beam, in both pulsing and continuous modes, can be deposited at the sapphire window for reasonable settings on the final deflection plates, H2 and V2. As described in Section 3.1.5, different settings in H2/V2 are required for peak ion current in Faraday cup 3 vs. peak deposit at the window.

Einzel lens 2 (L2) focuses the beam to pass through the aperture in the first element of the decelerator lens. Einzel lens 3 (L3) is set to zero in this setup. The decelerator lens can be used to vary Ba<sup>+</sup> deposit energy, which was done in [30], but in this work it acts as an Einzel lens with only the second element (D2) at voltage. It focuses the beam near the sample and Faraday cup 3 (there is no Faraday cup 2 in this setup). Faraday cup 3 measures the ion current during experiments, and is retracted when deposits are being made. Calibration of deposits using Faraday cup 3 is described in Section 3.1.5. Faraday cup 1 can be used for beam diagnostics, and is usually retracted.

To align the ion beam, L1 was first tuned to maximize ion current in Faraday cup 3, with L2, L3, and D2 set to zero. Since cup 3 is about 2 m away from L1, this approximately collimates the beam for passage through the E×B filter. The optimal value for L1 was found to be around -400 V relative to the 2000 V beam energy *consistent with Bill's SIMION – show?*. Next, L2 and D2 were fine-tuned together to achieve maximal current in cup 3. Finally, the straightness of the beam was checked by peaking ion current with deflection plates H1 and V1 on cup 3, as well as on cup W, which is an additional Faraday cup attached to the coldfinger in place of the sapphire window. Cup W is further described in Section 3.1.5.

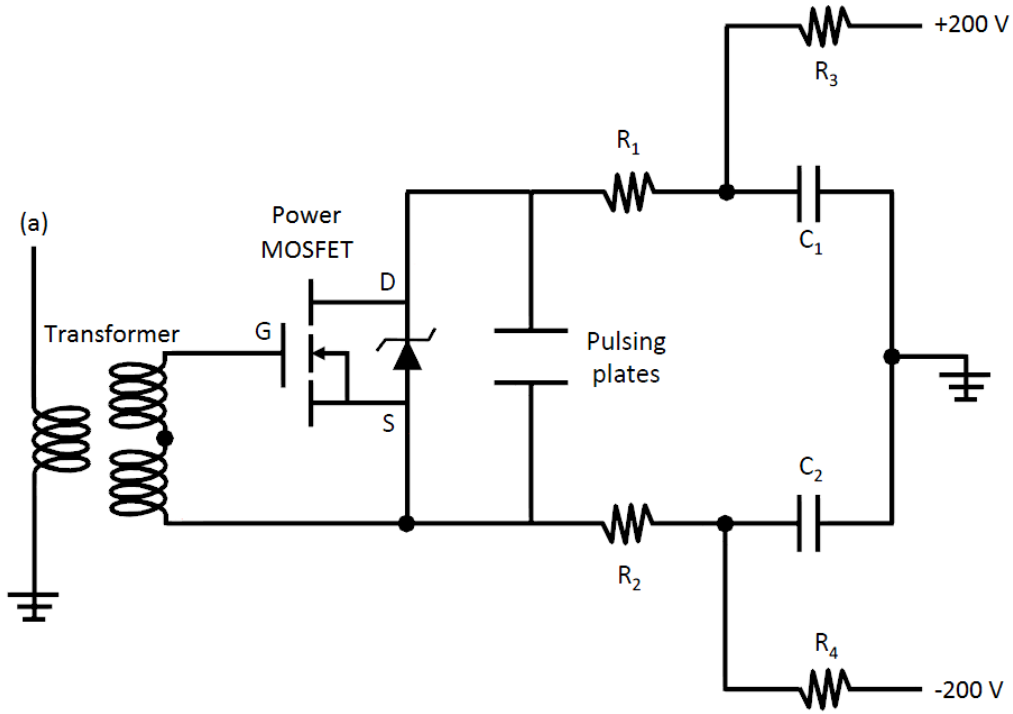


FIGURE 3.4. Pulsing circuit.  $R_1 = R_2 = 470 \Omega$ ,  $R_3 = R_4 = 20 \text{ k}\Omega$ ,  $C_1 = C_2 = 680 \text{ nF}$ . [30]

### 3.1.4. ION BEAM PULSING

When running in pulsing mode, the pulsing plates are normally set to 200 V and -200 V to deflect the beam, and are pulsed to 0 V for 1  $\mu\text{s}$  to pass a short pulse of ions straight forward. The pulsing circuit is shown in Fig. 3.4. Square waves, triggered by LabVIEW at 500 Hz, enter the circuit at (a). The transformed pulse triggers the MOSFET switch, which closes the circuit for the period of the pulse.

The induction plates are used to observe pulses during a deposit. Pulses just prior to a deposit can be observed by cup 3 (as well as the induction plates) for a measurement of ion current in the pulses. eV Products pre-amplifiers convert the ion current to voltage signals, which are recorded on a digital oscilloscope. An example of raw oscilloscope traces

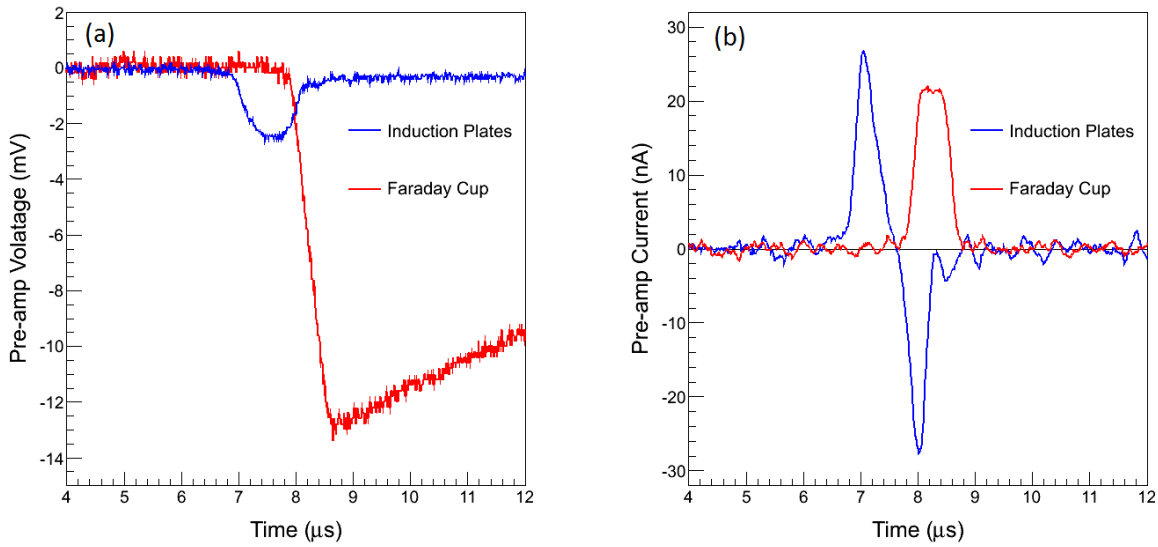


FIGURE 3.5. Raw (a) and shaped (b) pulse signals from induction plates and cup 3. The raw induction signal appears small because it is a less sensitive pre-amp (accounted for in shaping).

of Faraday cup 3 and induction plate signals are shown in Fig. 3.5(a). The pre-amp output voltage is related to the input current according to Eqn. 10:

$$(10) \quad I = \frac{-(V_{out} + R_1 C \frac{dV_{out}}{dt})}{R_1 M}$$

$R_1 C$  and  $R_1 M$  are determined by putting a known square pulse into the pre-amp. First, the time constant of an exponential fit to the signal decay determines  $R_1 C$ , and then  $R_1 M$  is determined by matching this shaped signal to the original square pulse. Actual currents in the induction plates and cup 3 are shown in Fig. 3.5(b). The induction signal is positive as ions are approaching the sensitive plate, and an equal but negative signal is seen after the ions pass through. The Faraday cup stops the ions, so it produces only a positive induction signal as ions approach it.

Pulsing data also provides confirmation that the beam is composed of  $\text{Ba}^+$ . The time between the center of the pulsing plate voltage overlap and the center of the pulse measured by the Faraday cup, along with a measurement of the distance traveled, provides a velocity measurement of the ions. This distance was measured to be  $31.5 \pm 0.5$  cm from the center of the pulsing plates to the Faraday cup, and time-of-flight data, e.g. Fig. 3.6, give  $39.8 \pm 3.4$  amu for  $\text{Ar}^+$  and  $136.8 \pm 6.3$  amu for  $\text{Ba}^+$ , including an uncertainty on the time of flight of  $\pm 0.1 \mu\text{s}$ .

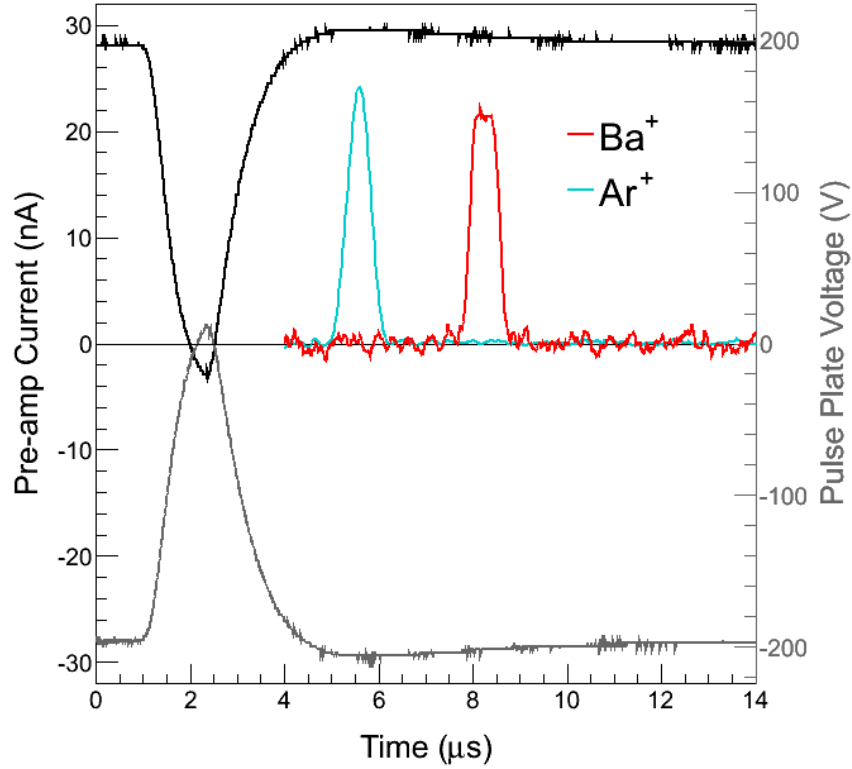


FIGURE 3.6. Arrival time of pulses at cup 3 vs. time of pulsing plate signal (black (+) and gray (-)) for  $\text{Ar}^+$  and  $\text{Ba}^+$ .

### 3.1.5. CALIBRATION OF ION DEPOSIT

To calibrate the signal at cup 3 to an ion density at the sapphire window, another Faraday cup (cup W) is attached to the cold finger in place of the sapphire window. The ratio of

between ion current in cup 3 and cup W is measured ( $\equiv f$ ). Then, knowing the radius of the entrance aperture in cup W lets one determine the ion density per pulse at the sapphire window:

$$(11) \quad \frac{\text{ions}}{\text{pulse} \times m^2} = \frac{Qf}{eA}$$

where  $Q$  is the charge/pulse at cup 3,  $A$  is the area of cup W, and  $e$  is the elementary charge. The voltages on the final deflection plates H2 and V2 are also determined to optimize the signal in cup W. In later experiments, these differed from the values for maximum cup 3 signal by about 70 V in H2 and 60 V in V2, corresponding to about 4 mm in x and y position at cup W, indicating that some drift in optimal ion beam component settings occurred over time.

### 3.2. BA GETTER SOURCE

A BaAl<sub>4</sub> getter, manufactured by SAES, can be inserted on a bellows to emit toward the sapphire window, shown in Fig. 3.7. When heated, the getter emits neutral Ba with minimal Ba<sup>+</sup>. Getters were used extensively in previous work [31] for measuring the absorption of Ba in SXe with large Ba deposits, and in identifying emission peaks. A getter was used briefly in this work in identifying the 619-nm fluorescence peak, as described in Section 5.2. The barium getters used in [31] were exothermic BaAl<sub>4</sub>-Ni flash getters. The getter used here is an endothermic BaAl<sub>4</sub> type, designed for more controlled Ba emission.

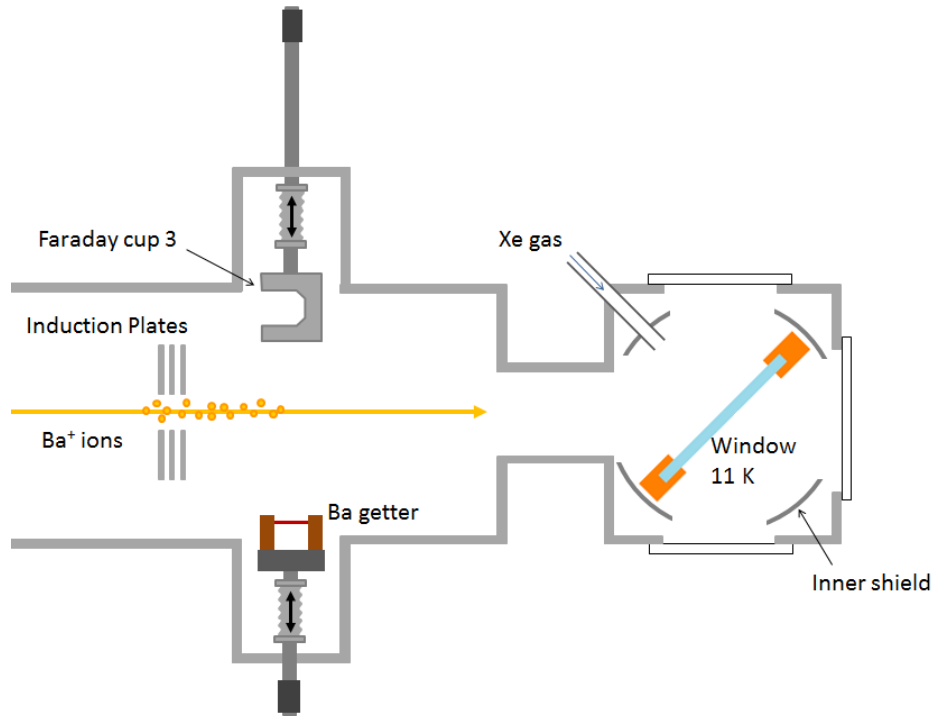


FIGURE 3.7. Apparatus near sapphire window, including Ba getter, Faraday cup 3, induction plates, and Xe gas inlet.

### 3.3. SAMPLE DEPOSITION

The  $\text{Ba}^+/\text{Ba}$  is co-deposited with ultra-pure Xe gas onto a cold sapphire window. Sapphire has good thermal conductivity at low temperature and good optical transparency in the visible. The window is held in a copper mount attached to a coldfinger and is tilted at  $45^\circ$  to allow access of the ion beam and Xe gas, as well as the excitation laser and collection optics. To begin a deposit, Xe gas is flowed toward the window via a leak valve. Cup 3 is then retracted and the ion beam is pulsed, depositing  $\text{Ba}^+$  ions into the SXe matrix as it grows. Cup 3 is then replaced, and the Xe leak stopped.

SXE matrix deposition rate can be measured by interference fringes in a laser reflected against the front surface of the sapphire window, as shown in Fig. 3.8. Fringes for SXe deposition at 52 K and 11 K are shown in Fig. 3.9(a) for the leak rate used in this work.

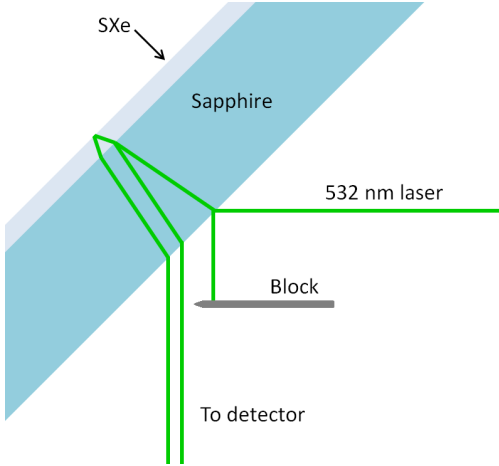


FIGURE 3.8. Setup for measuring SXe deposition rate by interference fringes.

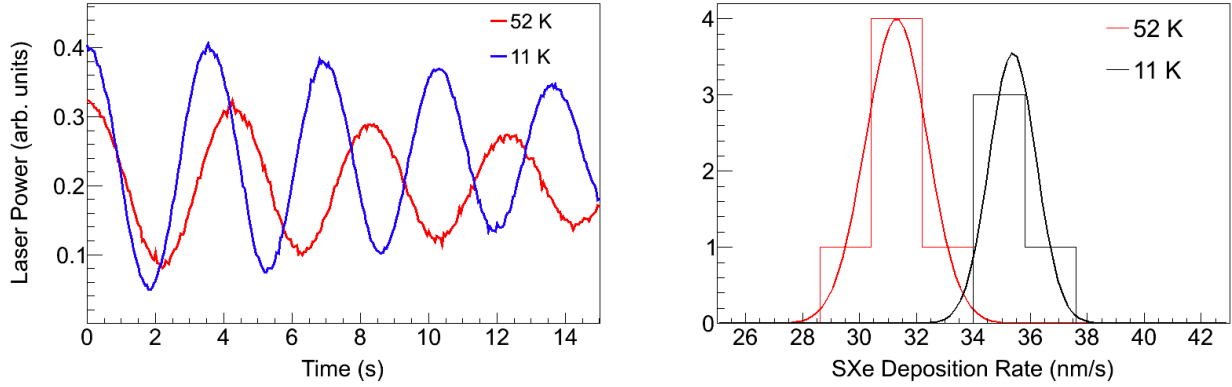


FIGURE 3.9. Interference fringes for the same Xe gas leak rate deposited on the sapphire window at 11 K and at 52 K.

The refractive index of SXe has a negligible dependence on temperature between 50 and 30 K [32], so these can be compared directly. A distribution of SXe deposition rate measurements from several deposits is shown in Fig. 3.9(b). A somewhat lower rate is observed at 52 K,  $31.3 \pm 0.44(\text{stat}) \pm 0.31(\text{sys}) \text{ nm/s}$ , vs.  $35.4 \pm 0.41(\text{stat}) \pm 0.35(\text{sys}) \text{ nm/s}$  at 11 K. Statistical errors are  $\sigma/\sqrt{N}$  where  $\sigma$  is the standard deviation of the Gaussian fits to the distributions in Fig. 3.9(b), and  $N$  is the number of entries. Systematic errors come from propagating an uncertainty on the angle between the laser and sapphire window of  $\pm 2^\circ$ .

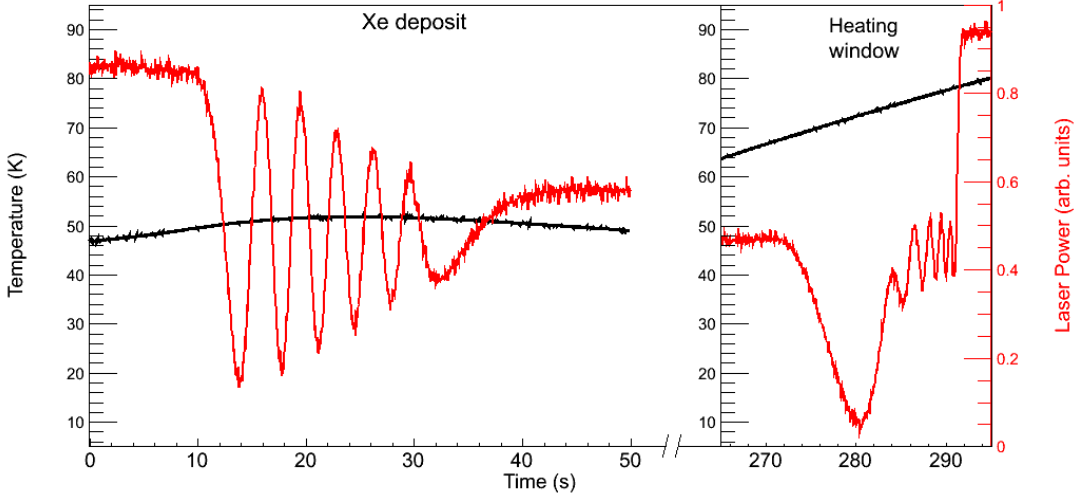


FIGURE 3.10. (a) Interference fringes of a deposit at 52 K and of its subsequent evaporation when heating the sapphire window, and (b) distribution of SXe deposition rates calculated from fringe period of several measurements.

To evaporate a sample, the window is heated to 100 K. Fringes appear during this process as well. The full set of fringes for a deposit at 52 K and its evaporation when heated is shown in Fig. 3.10, along with the window temperature. This shows that the SXe evaporates between 73 K and 78 K. The same number of fringes appear in the deposit and the evaporation, indicating that the lower deposition rate at around 50 K is not due to simultaneous evaporation. The variance in temperature during the deposit is due to the heater cycle. Note that these Xe deposits were longer than for a typical deposit during a fluorescence experiment, in order to observe several fringes.

where sh'ew put this? sh've? these numbers are apparently wrong anyway Using the 10 K SXe density of 3.780 g/cm<sup>3</sup> [38] and a typical Ba<sup>+</sup> ion current density of 1.6 nA/mm<sup>2</sup> at the sapphire window, Re-do this, ala procedure in thought\_process.pptx, since you don't claim 37 nm/s anymore: 5 nm/s any other instances? and 37 nm/s correspond to Xe:Ba ratios of about  $8.7 \times 10^3$  and  $6.4 \times 10^4$  respectively. Xe leak rates above 37 nm/s result in rapid frosting of the SXe matrix, which causes blurring of the image and high laser scatter.

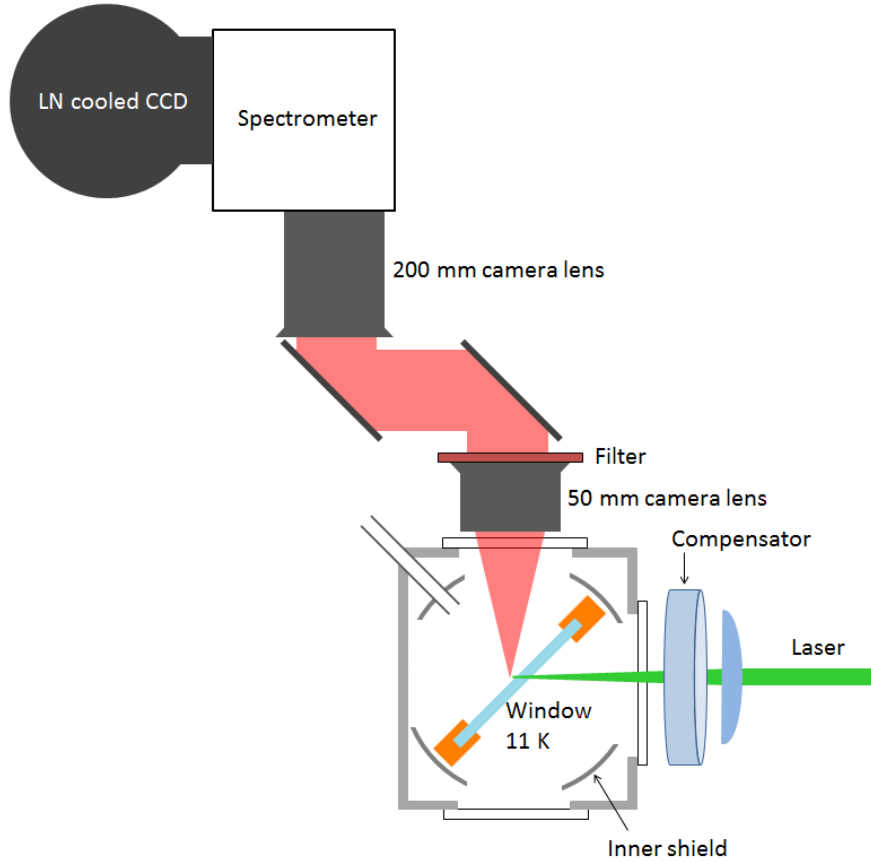


FIGURE 3.11. Apparatus in spectroscopy region, including optics for excitation, fluorescence collection, spectroscopy and detection.

### 3.4. LASER EXCITATION

Green to yellow laser excitation is done with a Coherent 599 dye laser, pumped by the 514-nm line of a Lexel 3500 Ar ion laser. Rhodamine 110 (R110) dye is used for the 542 - 566 nm wavelength range, and Rhodamine 6G (R6G) for the 567 - 590 nm range. Another Coherent 599 dye laser with Coumarin 480 (C480) dye is used for blue excitation, which is pumped by a Kr ion laser. The Coherent 599 dye lasers are used with birefringent filters for wavelength tuning, but without etalons, since the broad absorption of Ba in SXe does not require single-mode laser excitation.

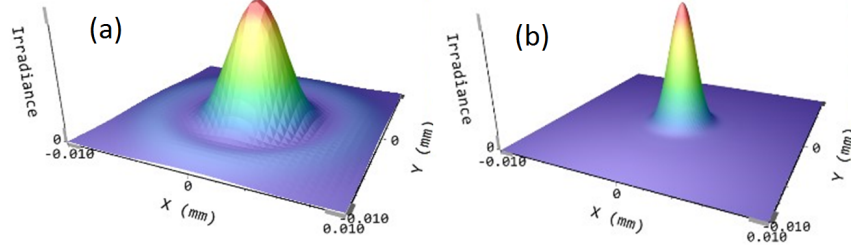


FIGURE 3.12. Calculated minimum laser spot size distributions, with wavelength 570 nm and unfocused waist  $w = 7$  mm, for (a) bi-convex  $f = 7$  cm lens, and (b) aspherical  $f = 7.9$  cm lens.

A lens focuses the laser into the cryostat from the side, shown in Fig. 3.11. Initial work, spectroscopy (Chapter 4) and some imaging, was done using a bi-convex, which produced spherical aberration near the laser focus. This effect does not affect the results in Chapter 4, where semi-focused beam waists of 100-1000  $\mu\text{m}$  were used. However, spherical aberrations caused the minimum beam waist to be about twice that of the diffraction limit. To approach the diffraction limit in imaging small numbers (Chapter 5), a 7.9-cm focal length aspherical lens was used. A comparison of the minimum spot sizes for these two lenses, calculated by David Fairbank at Thorlabs, is shown in Fig. 3.12.

To correct for astigmatism introduced by the tilted sapphire window, compensating astigmatism is introduced by a fused silica optical flat of 1 cm thickness, placed after the lens, tilted on the y-axis (the laser is along the z-axis, and the sapphire window is tilted on the x-axis). The proper angle for the compensator was determined to be about  $10^\circ$  from normal by a ray matrix calculation [33]. The effect of the SXe layer is negligible since its thickness is only about half a micron in a typical fluorescence experiment. With the compensator, overlapping minimum spot sizes of  $2.06 \mu\text{m}$  and  $2.66 \mu\text{m}$  are calculated for x and y, respectively. To observe the astigmatism and the effect of the compensator, the relative position of the x- and y-focus was observed by imaging 619-nm Ba fluorescence from a large deposit of  $\text{Ba}^+$  in SXe, with a varying laser focus. For each z-position of the laser focusing lens, an

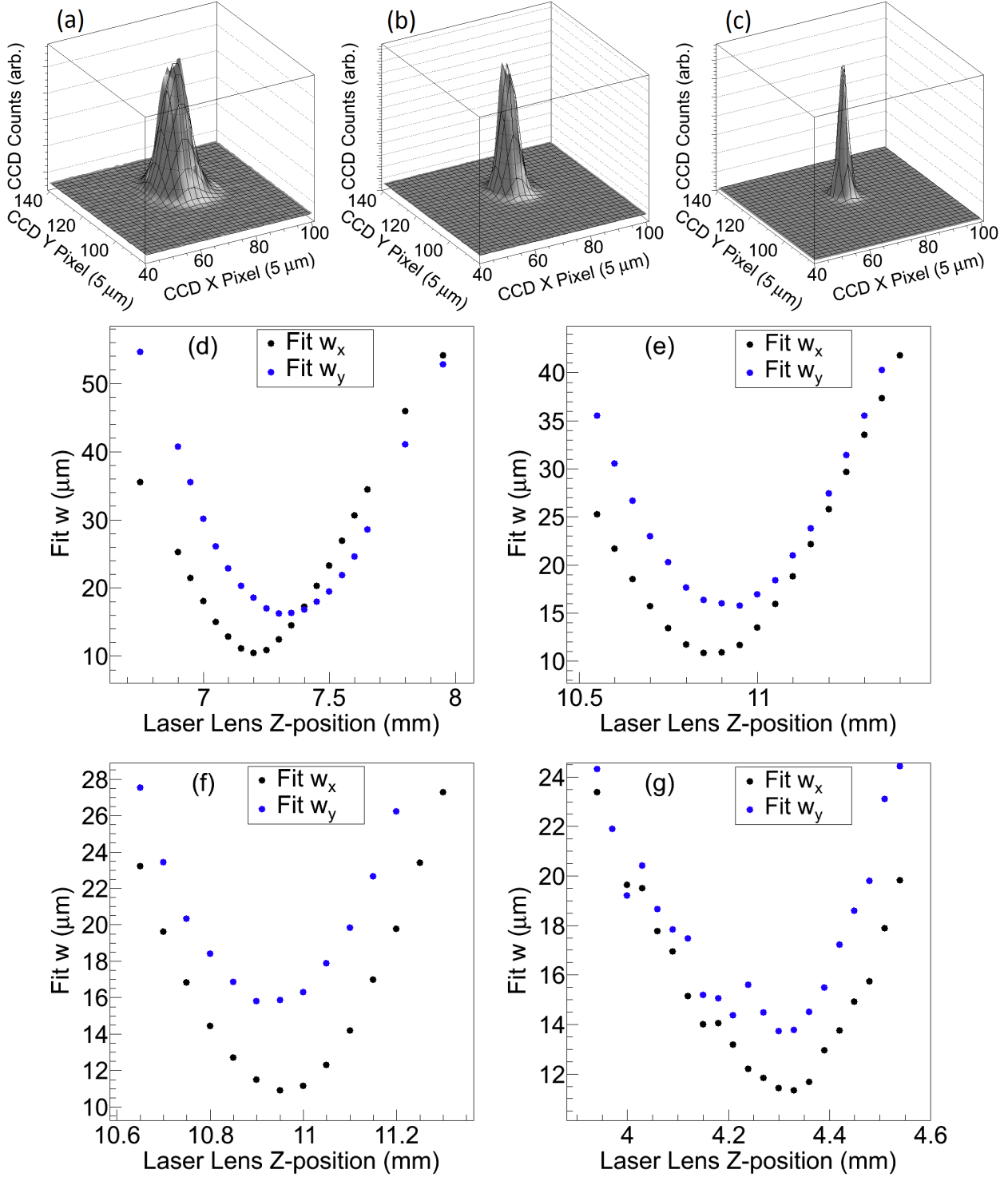


FIGURE 3.13. Example 2D Gaussian fits (black grid lines) with varying laser focus (a,b,c), and fit waists  $w_x$  (black) and  $w_y$  (blue) vs. laser focus lens position with (d) no compensator, and with compensator at about (e)  $10^\circ$ , (f)  $13^\circ$ , and (g)  $11^\circ$ .

image was taken, and a 2D Gaussian fit determined the x and y beam waists,  $w_x$  and  $w_y$ . Example fits to the 619-nm fluorescence for three laser focus positions, using the astigmatism compensator at  $10\pm1^\circ$ , are shown in Fig. 3.13(a,b,c). Gaussian fit values for  $w_x$  and  $w_y$  are plotted vs. laser focus position with (d) no compensator, and with the compensator at (e)  $10\pm1^\circ$ , (f)  $13\pm1^\circ$ , and (g)  $11\pm1^\circ$ . With no compensator (d), the focal positions for x and y are measured to be  $127.6\pm2.5 \mu\text{m}$  apart.  $10\pm1^\circ$  (e) and  $13\pm1^\circ$  (f) can be seen to under- and over-shoot the optimal angle, respectively.  $11\pm1^\circ$  (g), which was used in imaging experiments, is near optimal, i.e. the x and y foci are consistent to within  $45 \mu\text{m}$ .

### 3.5. COLLECTION OPTICS

Fluorescence is collected above the cryostat (Fig. 3.11). A 50 mm Nikon camera lens collimates the light, and a fluorescence filter sits on top of it. A band-pass filter is used for imaging, and a Raman filter was used for spectroscopy. The fluorescence then reflects off two steering mirrors, and is imaged by a 200 mm Nikon camera lens onto a Roper Scientific liquid-nitrogen-cooled CCD, with a magnification of 4. The CCD has a quantum efficiency of 90% in the visible, and in slow ADC mode, records one count per two photons collected. At the set point of  $-100^\circ\text{C}$ , dark counts are negligible.

The CCD has a removable Princeton Instruments imaging spectrometer. With this attached, the 200 mm camera lens focuses the light onto an inlet slit, which is then imaged by the spectrometer onto the CCD after reflecting off a diffraction grating. The 0-order reflection of the grating provides an image for alignment, and the grating can be tilted to distribute the 1<sup>st</sup>-order reflection across the horizontal CCD pixels for doing spectroscopy.

When a 1" diameter filter is used, the imaging system has a solid angle collection of about 1.5%. Each additional component in the collection optics, listed in Table 3.1, contributes

some loss, resulting in a total collection efficiency ( $\epsilon_c$ ) of  $2.4 \times 10^{-3}$  with the spectrometer, and  $4.8 \times 10^{-3}$  without. The spectrometer also limits the system to an f-number of 4, though this is not limiting in this setup.

TABLE 3.1. Factors contributing to optical collection efficiency. Total  $\epsilon_c$  includes 1.5% solid angle collection.

Component	Efficiency
Cryostat Window	0.99
Camera Lens 50 mm	0.89
Camera Lens 200 mm	0.91
Steering Mirrors ( $\times 2$ )	0.95
CCD Quantum Efficiency	0.90
Filter	0.98
Counts per Photon (CCD)	0.22
Spectrometer	0.5
	$\epsilon_c(\text{w/o spectrom.}) = 2.1 \times 10^{-3}$
	$\epsilon_c(\text{w/ spectrom.}) = 1.1 \times 10^{-3}$

To limit laser exposure to only the time of CCD exposure, a laser shutter was linked to the camera exposure with a LabVIEW program. This program also recorded laser power via a calibrated pickoff, as well as the temperature of the coldfinger near the sapphire window during observation.

### 3.6. VIBRATIONS AND EFFECTIVE LASER REGION

Relative vibrations between the laser and sapphire window affect the number of Ba atoms exposed, increasing the effective laser spot size. This was studied by observing the position of a “dust spot” (a highly scattering feature on the sapphire window) relative to the position of the laser in an image on time scales down to 50 ms. An example of an image from this experiment is shown in Fig. 3.14. The 570-nm dye laser was somewhat de-focused, and the dust spot was illuminated by a de-focused 657 nm diode laser. For each frame, 2D Gaussian functions were fit to locate the center of the laser spot and the dust spot in order to measure their relative position. The fit for the laser spot was restricted in y so that it was

not affected by the bulk sapphire fluorescence path. The distances in x and y between the dust spot and laser are plotted for each 50-ms snapshot in Fig. 3.15(a). The distribution shows a correlation between x and y. To calculate an effective laser spot size due to this vibration, each difference ( $x,y$ ) between laser and dust spot was used as the center of a 2D Gaussian, each with  $w_x = 2.06 \mu\text{m}$  and  $w_y = 2.66 \mu\text{m}$  to represent the laser spot. Such Gaussian functions were summed for all points to produce a distribution of summed laser exposure, shown in Fig. 3.15(b). The area enclosed by a  $1/e$  contour then represents the total exposed area, while signal at a given moment is emitted from the laser spot size. This leads to two definitions for the number of ions in the laser region (see Eqn. 11), and thus the upper limit on the number of atoms: average atoms exposed is defined by the laser spot size, and total atoms exposed is defined by the total region covered due to vibrations. Note that the factor between average and total areas depends on the laser spot size. The factor is about 4.7 for  $w_x \times w_y = 2.06 \mu\text{m} \times 2.66 \mu\text{m}$ , and about 3 for  $w_x \times w_y = 5 \mu\text{m} \times 5 \mu\text{m}$ .

The aforementioned is the most concerning vibration to understand. Vibration of the laser itself is included in that study. Vibration of the collection optics will affect the imaging resolution, but not the number of atoms being observed. These vibrations were minimized by stable mounts.

### 3.7. LASER SCANNING

In order to obtain images of separated single atoms, the laser focusing lens was attached to motorized translation stages which scanned the laser position by scanning the lens in x and y, shown in Fig. 3.16. These stages sat atop a manual z-translation stage for laser focusing. An extension of the aforementioned LabVIEW program coordinated movement of

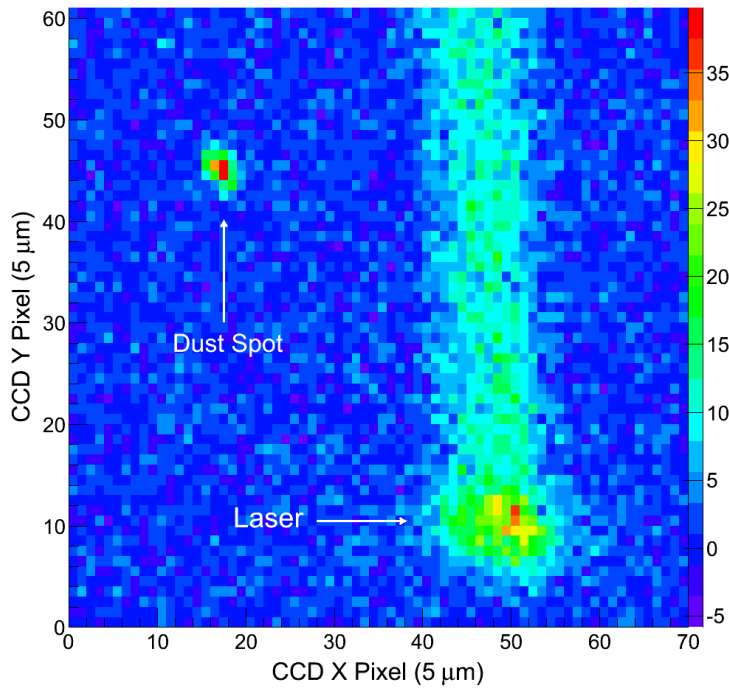


FIGURE 3.14. Example image of dust spot and laser during observation of cryostat vibrations.

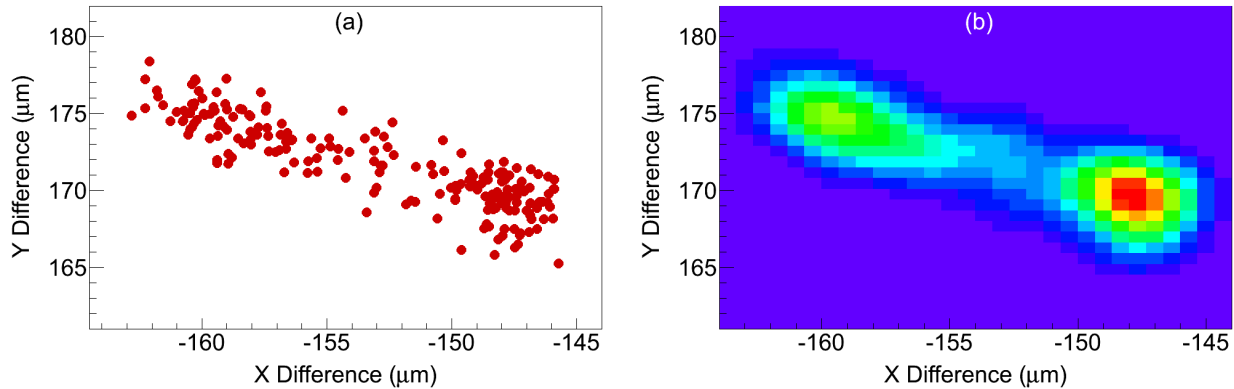


FIGURE 3.15. Cryostat vibration measurements based on relative position of dust spot vs. laser on sapphire window in 50-ms snapshots (a), with 2D Gaussians of  $w_x \times w_y = 2.06 \mu\text{m} \times 2.66 \mu\text{m}$  overlaid on each point to represent total laser exposure vs. position (b).

these stages such that x or y position was stepped in between CCD frames, and each frame then corresponded to a position in a laser scan grid.



FIGURE 3.16. Asphere laser focusing lens mounted to motorized Newport translation stages for laser scanning.

*The stages used in this work were Newport AG-LS25, which are driven by piezoelectric motors, but without accurate position feedback. As a result, some inconsistency in position reproducibility was observed. The position of the focused laser, measured by the center of a 2D Gaussian fit to the image of the laser spot, is shown in Fig. [fig laser grid] for ... 2015-08-12 has one from chris where he did 2D gaus, but you should get that w/ them lined up from the start too, to separate init pos from inconsistency, and you need to quantify both*

## CHAPTER 4

# METHOD

### 4.1. WAVELENGTH CALIBRATION

Wavelength calibration of the spectrometer was done using three lasers whose wavelengths were first measured with a Burleigh Wavemeter: a red diode laser at 656.99 nm, a doubled Nd:YAG laser at 532.23 nm, and the C480 blue dye laser typically around 475 nm. These lasers were directed at the same position on the sapphire window, and their scatter was imaged along the same path as the Ba fluorescence. The WinSpec software applies the diffraction grating equation to calibrate each CCD pixel to a wavelength.

### 4.2. FITTING OF SPECTRA

Fitting of fluorescence spectra, with sums of peak-specific fit functions, was used to track peak heights in excitation spectra, annealing cycles, and bleaching. The center and width parameters of the functions were kept fixed, while the heights were the free fitting parameters. Center and width parameters for each peak were determined by fitting spectra where that peak is relatively large. Some fine-tuning was done to match slightly different shapes resulting from different excitation wavelengths.

#### 4.2.1. FITTING SPECTRA WITH GREEN EXCITATION

Example fits to spectra of  $\text{Ba}^+$  deposits for several different green excitation wavelengths are shown in Fig. 4.1. To incorporate the tail in the shape of the 577- and 591-nm peaks, an asymmetric function of the form  $A(1+\text{erf}(\frac{x-a}{\sigma_1})(1-\text{erf}(\frac{x-a}{\sigma_2}))$  was used, where  $a$  is the fixed center-defining parameter,  $\sigma_1$  and  $\sigma_2$  are fixed left and right width parameters, and

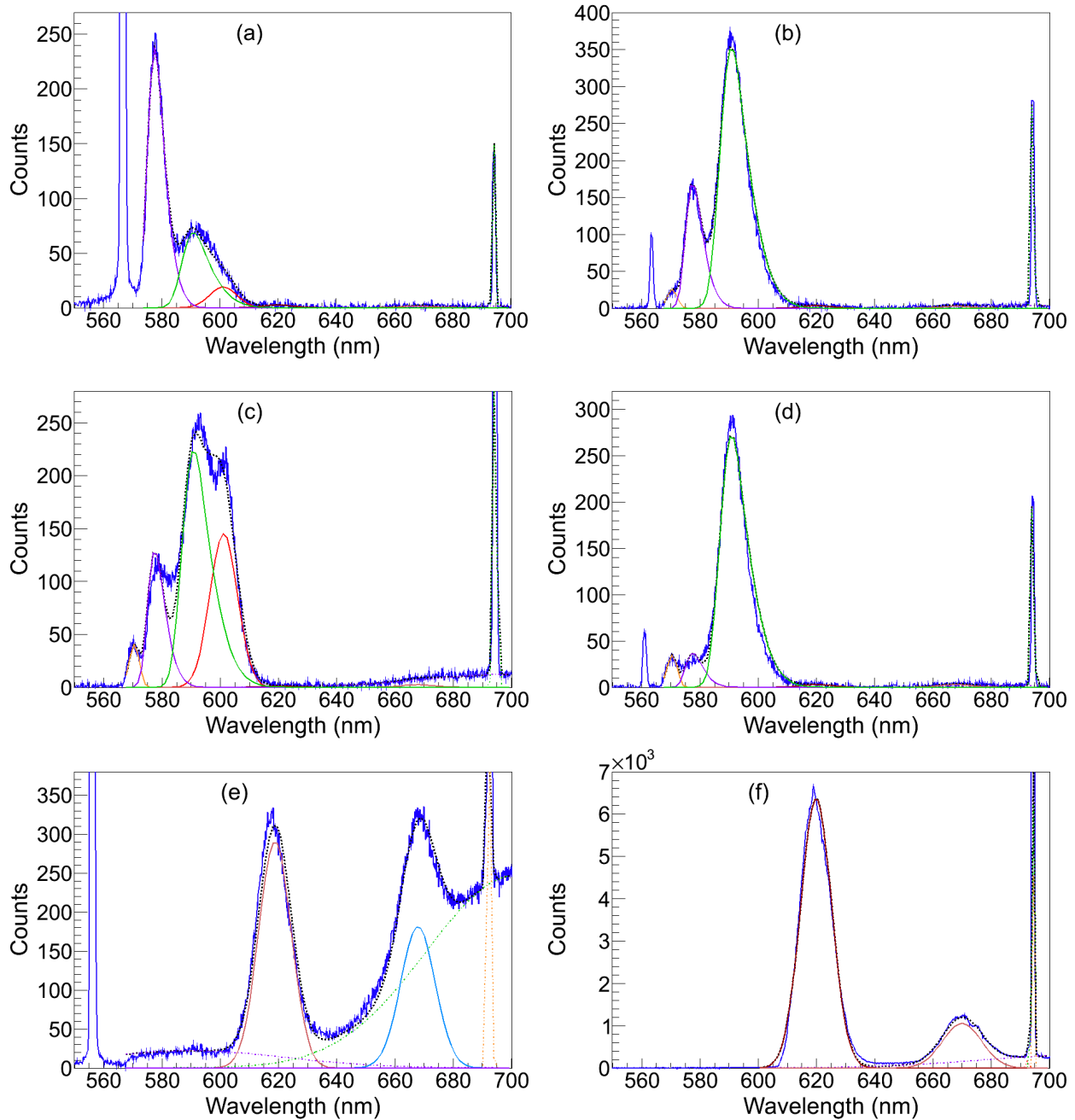


FIGURE 4.1. Example fits to spectra of  $\text{Ba}^+$  deposits with green excitation at (a) 566.6 nm, (b) 563.4 nm, (c) 546.3 nm, (d) 561.0 nm, (e) 555.9 nm, and (f) 567.3 nm. Laser scatter can be seen in the lower wavelengths for some figures, especially in (a) where it is on the edge of the Raman filter cutoff.

$A$  is the free amplitude parameter. The function  $\text{erf}()$  is an error function. The 570-, 601-, 619-, and 670-nm peaks were fit with Gaussian functions with fixed widths ( $\sigma$ ) of 1.7 nm, 4.7 nm, 5.3 nm, and 6.7 nm, respectively. Rather than attempting frame-by-frame background subtractions, additional Gaussians were fit to the broad and sharp background fluorescence. Two broad Gaussians centered at around 590 nm and 702 nm, and one sharp Gaussian at 694 nm, were chosen by fitting spectra of Xe-only deposits. These backgrounds and their excitation spectra are discussed in 4.3. The full fit, i.e. the sum of each contributing peak fit, is the dotted black line. Though the shapes do not match perfectly for all excitation wavelengths, the fits still follow the peak amplitudes well. Ba emission and excitation spectra results are discussed in Sec. 5.1.

#### 4.2.2. FITTING SPECTRA WITH BLUE EXCITATION

Example fits to spectra of  $\text{Ba}^+$  deposits for several different blue excitation wavelengths are shown in Fig. 4.2. Gaussian functions were used for 532-, 568-, and 575-nm peaks with widths ( $\sigma$ ) of 2.4 nm, 5.0 nm, and 0.7 nm, respectively. Lorentzian functions were used for the 553-, 592-, 635-, and 669-nm peaks with widths ( $\gamma$ ) of 1.7 nm, 13.8 nm, 10.4 nm. and 9.1 nm, respectively. Similar to spectra with green excitation, the background components were fit with two broad Gaussians centered at 546.0 nm and 703.3 nm, with respective  $\sigma$  of 49.0 nm and 30.5 nm, as well as one sharp Gaussian centered at 693.4 nm peak with  $\sigma$  of 0.5 nm. The fits around 478 nm (e.g., (c)) are not quite right, mainly due to a shift in central value of the 592-nm peak. However, fit values still follow respective peaks heights well. The 522- and 575-nm peaks are seen in (c), though the 522-nm peak is left out of the fitting range since it sits on the Raman filter cutoff. These spectra are discussed in Sec. 5.6.

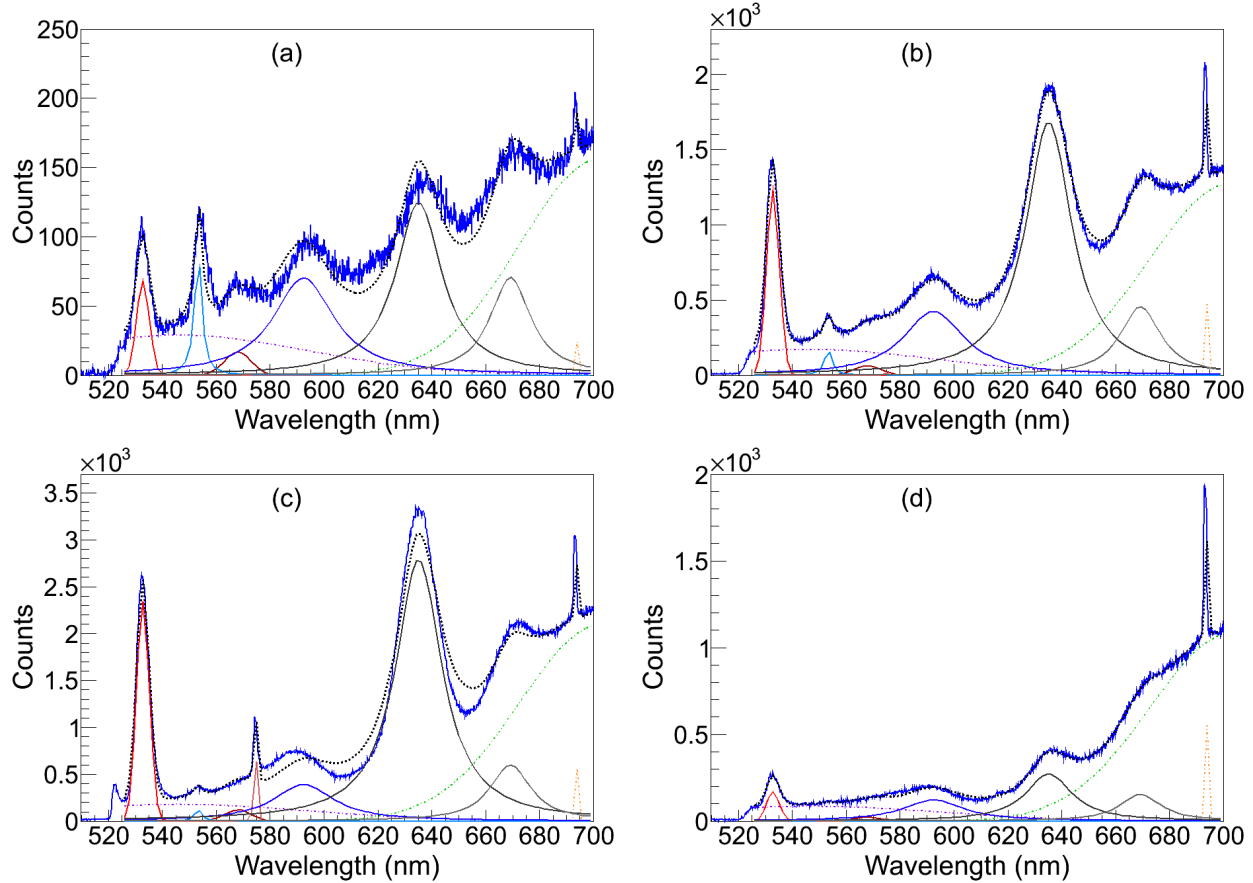


FIGURE 4.2. Example fits to spectra of  $\text{Ba}^+$  deposits with blue excitation at (a) 461.7 nm, (b) 468.2 nm, (c) 478.3 nm, and (d) 488.2 nm.

#### 4.3. OPTIMIZING SIGNAL-TO-BACKGROUND

One source of background emission was observed from the surfaces of the window. Its broad fluorescence is shown in Fig. 4.3(a) with a 610-nm Raman filter cutoff and 570.4 nm excitation, and its excitation spectrum is shown in Fig. 4.3(b) over the R6G dye range. The nature of this emission has not been determined, however a few features were identified. One was that the emission increased as the window temperature was decreased, down to about 100 K where it remained flat down to 11 K, shown in Fig. 4.4. Another feature of the surface background is that it bleaches with laser exposure. In order to reduce this background in imaging experiments, as well as to reduce run-to-run variation in the background due to

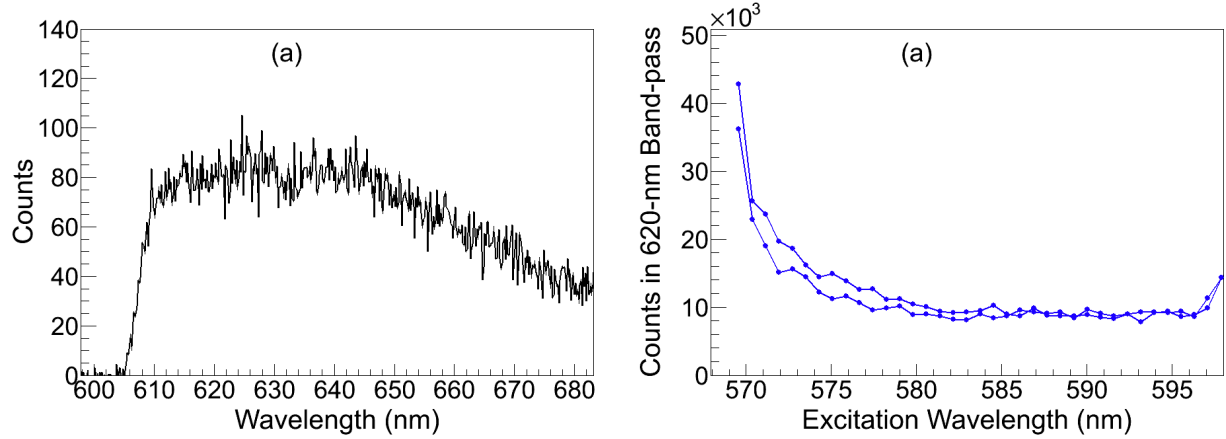


FIGURE 4.3. (a) Surface background emission spectrum w/ excitation at 570.5 nm, and (b) excitation spectrum through wavelengths in R6G dye range. The sharp drop in (a) around 608 nm is the Raman filter cutoff.

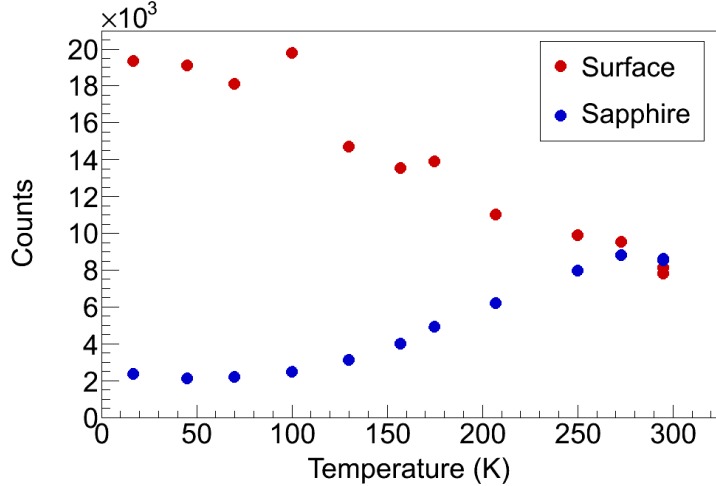


FIGURE 4.4. Temperature dependence of surface (red) and sapphire bulk (b) backgrounds.

bleaching, the sapphire window was pre-bleached for at least half an hour. Decay of the surface background emission, with intermittent observation during a pre-bleaching process, is shown in Fig. 4.5. For efficient pre-bleaching, the dye laser tuned to 580.5 nm for higher laser power, though the observation points in Fig. 4.5 are taken with the dye laser at 570 nm with the same laser power used in the following Ba imaging experiment. During imaging experiments, frequent Xe-only deposits were made in order to track surface background emission to establish proper background subtraction.

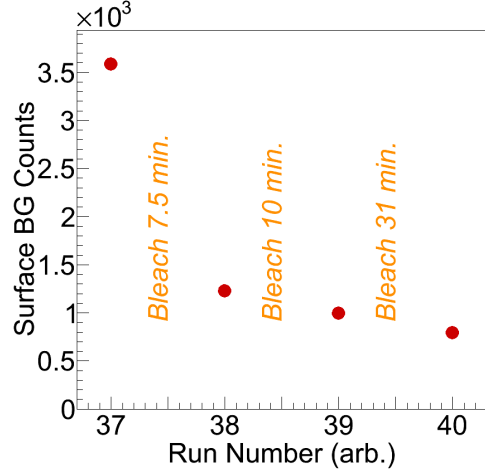


FIGURE 4.5. Decay of surface background emission during pre-bleaching of the sapphire window.

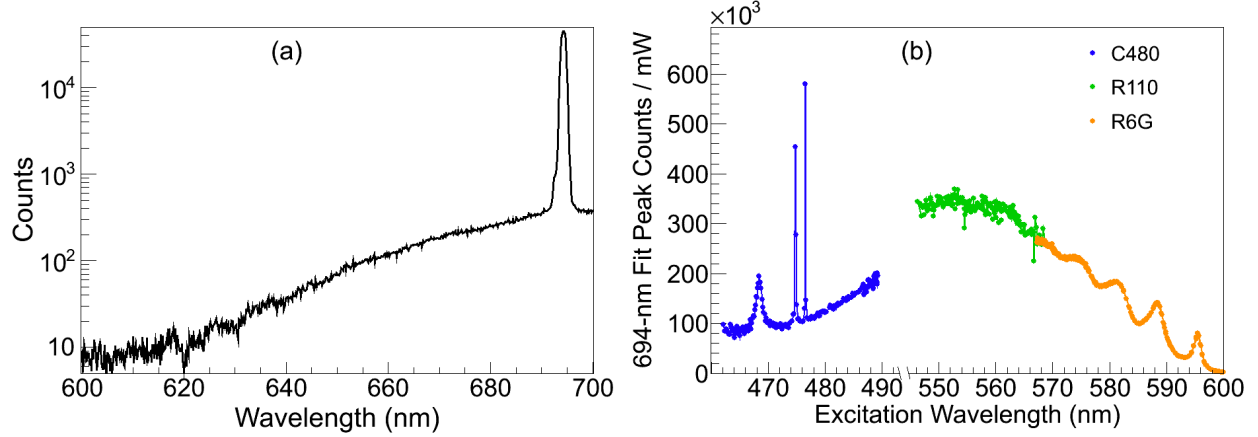


FIGURE 4.6. (a) Sapphire bulk emission with 562-nm excitation at 11 K, and (b) excitation spectrum of the sharp 694-nm emission peak using three different laser dyes. Due to different laser powers and exposure times, the R110 and R6G were scaled to match at their boundary.

Another source of background is fluorescence from the sapphire window bulk. A spectrum of this fluorescence with 562 nm excitation is shown in Fig. 4.6(a). The strong, sharp peak at 694 nm is a well-known  $^2E - ^4A_2$  emission in the  $d^3$  configuration of  $\text{Cr}^{3+}$  impurities in the sapphire bulk [34, 35]. An excitation spectrum for this peak is shown in Fig. 4.6(b) over the range all three dyes R6G, R110, and C480, using a sapphire window with relatively high  $\text{Cr}^{3+}$  content. Multiple features observed in the excitation spectrum, obtained by integrating

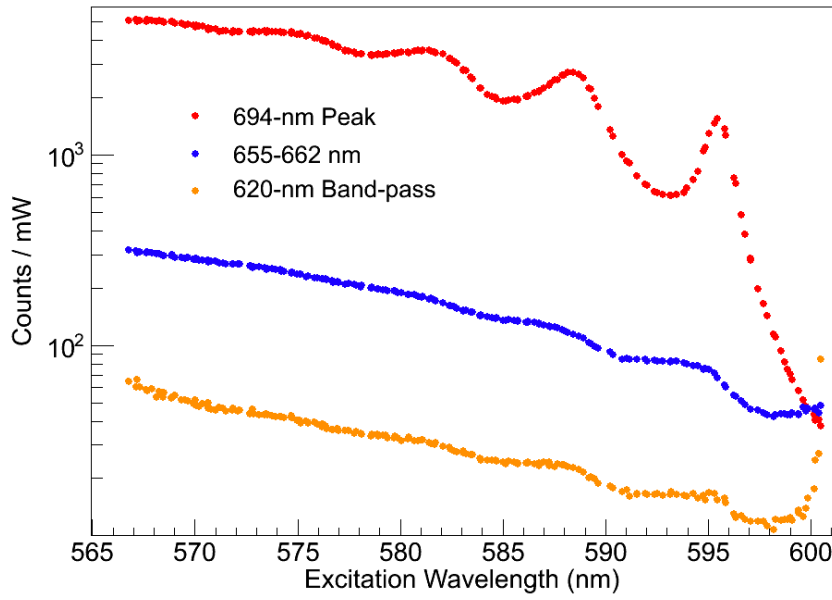


FIGURE 4.7. Excitation spectra for weaker sapphire bulk emissions (blue,orange) along with that of the strong 694-nm emission (red).

the 694-nm peak fit (Sec. 4.2) vs. excitation wavelength, are consistent with the absorption spectrum of Cr<sup>3+</sup> in sapphire at 77 K, including three sharp peaks in the blue at 468.4, 474.8, and 476.5 nm, as well as a broad absorption in the green/yellow, peaking around 550 nm, with vibrational peaks on the red tail [36, 37]. In addition to the 694-nm peak, a weaker and much broader emission is observed, along with three weak peaks around the 619-nm Ba peak region, also from the sapphire bulk. Excitation spectra for these fluorescence components are shown in Fig. 4.7 for the R6G dye range. In this experiment, the laser was de-focused to about  $w = 200 \mu\text{m}$ , and the emission observed was had contribution of the surface background as well as the bulk sapphire emission. This is negligible for the prominent 694-nm peak, however the rising features of the surface background emission, near 600 nm and 567 nm, can be seen in the excitation spectra of the weaker components (blue, and especially orange curves in Fig. 4.7). Nonetheless, observation of the same vibrational peaks as in the 694-nm peak demonstrates that the broad emission and weak peaks in the

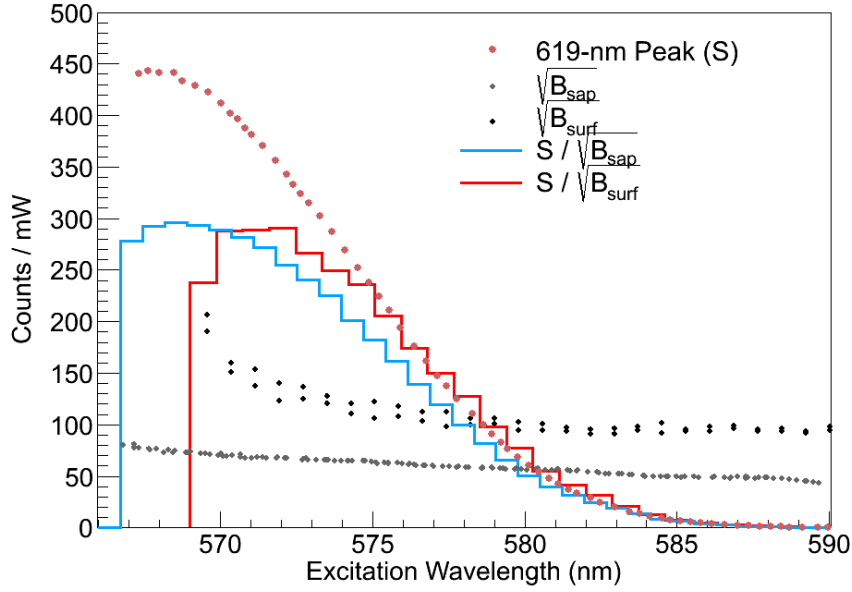


FIGURE 4.8. Optimization of signal to background with the 619-nm fluorescence signal ( $S$ ) for emission from the surface background ( $B_{\text{surf}}$ , red) and for the bulk sapphire emission ( $B_{\text{sap}}$ , cyan).

620 band-pass (Fig. 4.6(a)) are also due to  $\text{Cr}^{3+}$  in the sapphire. Commercially available c-plane quality sapphire windows contain low concentrations of  $\text{Cr}^{3+}$ . Sample windows of 0.75" diameter and 0.02" thickness from a few companies were tested, and those from Meller Optics produced the lowest sapphire bulk emission in the 620-nm band-pass region.

Consideration of signal-to-background ( $S/\sqrt{B}$ ) guided the choice of 570 nm for excitation of the 619-nm fluorescence.  $S/\sqrt{B}$  for emission passed by the 620-nm band-pass filter is plotted vs. excitation wavelength in Fig. 4.8 for the surface background ( $B_{\text{surf}}$ ) as well as for the sapphire bulk emission ( $B_{\text{sap}}$ ). The peak in  $S/\sqrt{B}$  represents the optimal excitation wavelength respective to each of the two background sources. Around 568.5 nm is optimal vs. the sapphire emission, and around 571 nm is optimal vs. the surface background emission. 570 nm, which was used in sensitive imaging experiments, is nearly optimal in both cases.

## CHAPTER 5

### RESULTS: SPECTROSCOPY

The spectroscopy of Ba in SXe was studied in detail beyond that reported in [30, 31], with the goal of imaging single Ba atoms. Emission and excitation spectra are analyzed in 5.1, with particular interest in the origin of the 619-nm peak in 5.2. Studies of temperature and bleaching effects in 5.3 and 5.4 aid in determining optimal conditions for observation. Finally, candidate emission lines for Ba<sup>+</sup> in SXe are discussed in 5.6.

#### 5.1. EXCITATION AND EMISSION OF BA IN SXE

Deposits of Ba in SXe absorb primarily between 540 nm and 570 nm. An absorption spectrum, obtained by observing absorption of white light by a large Ba deposit at 10 K, is shown in Fig. 5.1. Significant broadening, as well as a 4-nm redshift of the central peak, occur relative to the vacuum  $6s^2 \ ^1S_0 \rightarrow 6s6p \ ^1P_1$  absorption value of 553.5 nm. Initial discovery of this absorption and emission was done with the neutral Ba getter source [19, 30, 31]. The emission spectrum in Fig. 5.1 was obtained by 557-nm excitation of a Ba<sup>+</sup> deposit, made at 45 K and observed at 11 K. Observation of the same 577- and 591-nm fluorescence peaks from Ba getter deposits demonstrates that these peaks are emission of neutral Ba, and also demonstrates some neutralization of the ions [19, 30, 31]. The fraction of ions neutralized has not been determined.

Deposition at temperatures higher than 10 K and exploration of more excitation wavelengths have led to discovery of emission peaks beyond the 591- and 577-nm peaks reported in [30] and [31]. Emission spectra for selected excitation wavelengths are shown in Fig. 5.2(a) for a deposit made at 44 K and observed at 11 K.

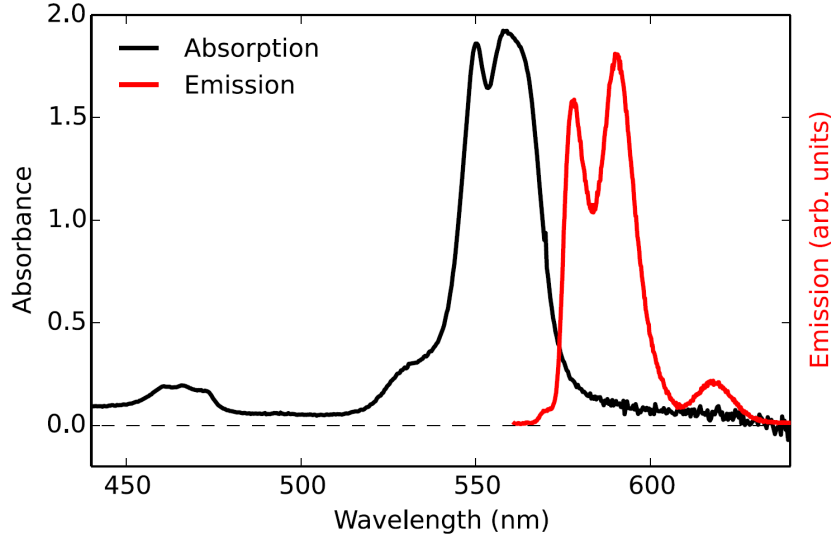


FIGURE 5.1. Absorption and emission spectra of neutral Ba in SXe. The absorption is of a Ba getter deposit at 10 K, and the emission is of a (neutralized)  $\text{Ba}^+$  deposit, deposited at 45 K and observed at 11 K with 557 nm excitation. From [19].

Excitation spectra, shown in Fig. 5.2(b), were produced by scanning the dye laser and measuring the magnitude of each fluorescence peak vs. excitation wavelength. For each frame, the spectrum was fit with a sum of peak-specific fit functions, where function shape parameters were fixed (centers and widths) and magnitudes were allowed to float. Fitting is described in Section 4.2.1. The discontinuity around 566 nm for the 619- and 670-nm peaks is the boundary between the scan range of different laser dyes. R6G dye was used for higher wavelengths and R110 for lower wavelengths. Curves were scaled for visibility on the same plot. Excitation was done using laser waists ( $w$ ) of (1)  $w = 7 \text{ mm}$  for the 570-, 577-, 591-, and 601-nm peaks, (2)  $w = 1000 \mu\text{m}$  for the 619- and 670-nm peaks in the R110 range, and (3)  $w = 200 \mu\text{m}$  for the 619- and 670-nm peaks in the R6G range. Due to these different laser waists, as well as different deposit sizes, curves for the R6G segments (619- and 670-nm peaks) required special scaling to line up with their respective R110 segments. This scaling

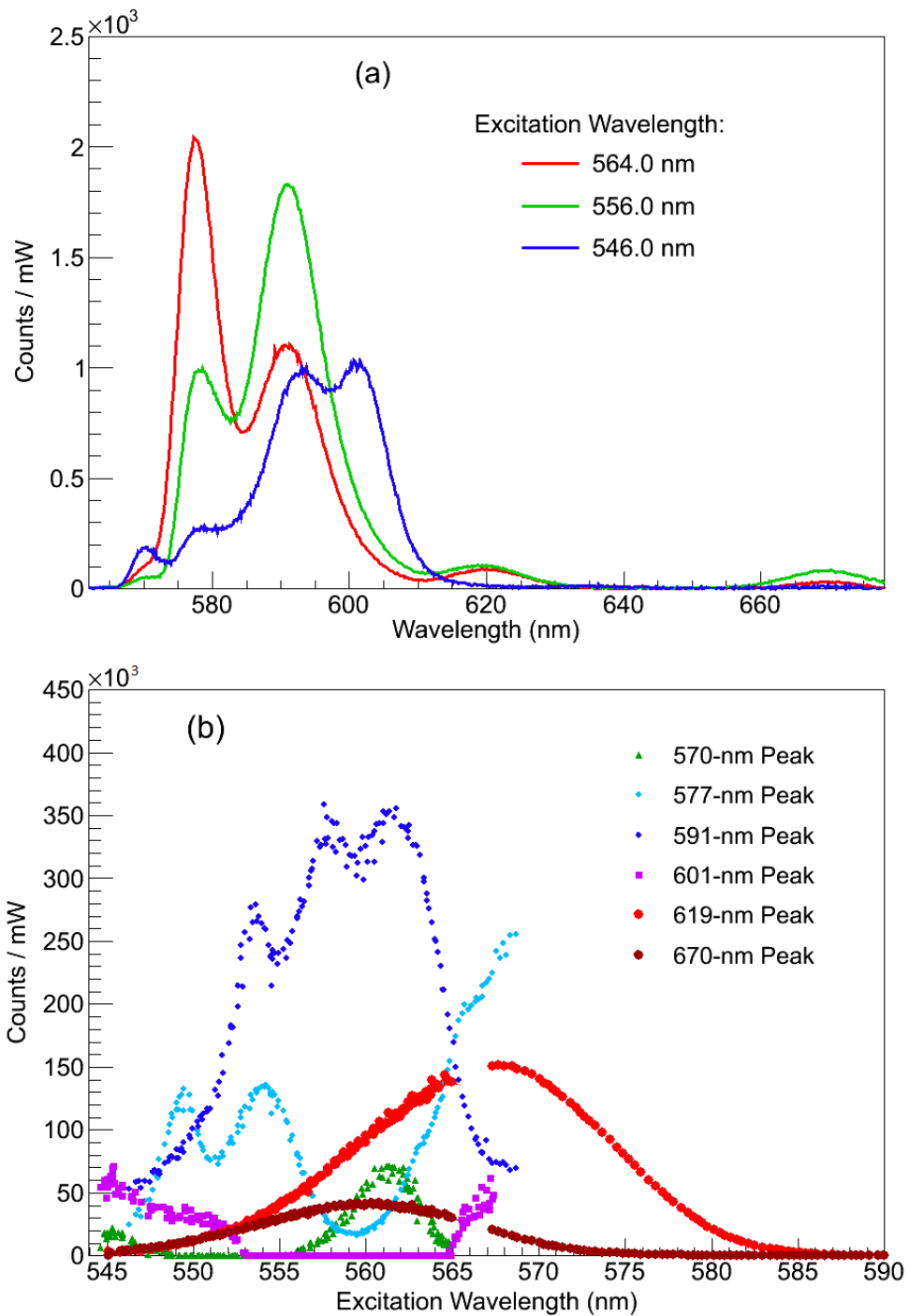


FIGURE 5.2. (a) Background-subtracted fluorescence spectra for a few different excitation wavelengths, and (b) excitation spectra for all observed Ba fluorescence peaks. Magnitudes in (b) have been scaled for visibility on the same plot. Exposures are 1 s.

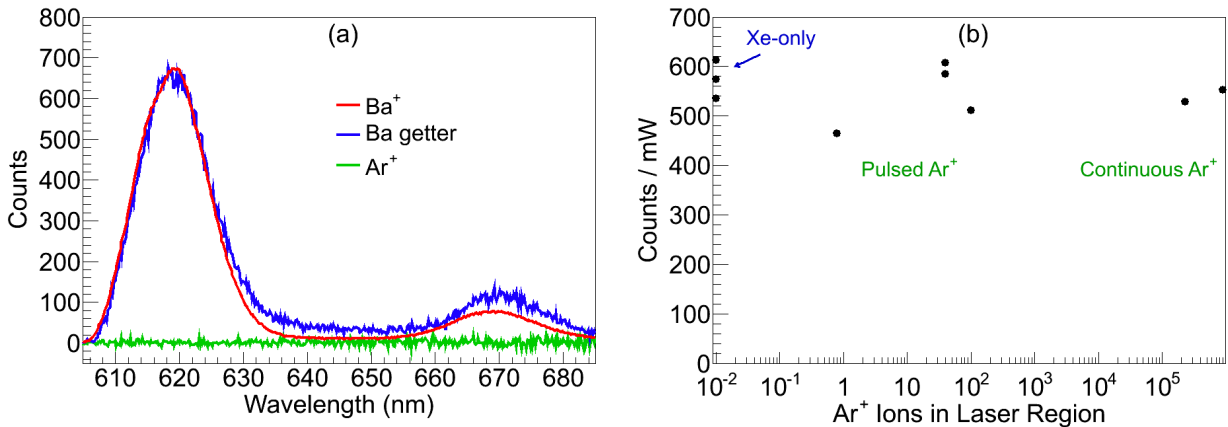


FIGURE 5.3. Comparison of signal observed for deposits with the  $\text{Ba}^+$  ion beam (red), Ba getter (blue), and  $\text{Ar}^+$  ion beam (green) (a), and signal through 620-nm band-pass from deposits of small to large numbers of  $\text{Ar}^+$  ions in SXe.

was slightly different between the 619- and 670-nm peaks, likely due to different relative populations of those sites on the different deposits.

## 5.2. 619-NM PEAK IDENTIFICATION

The 619-nm peak, as well as the 670-nm peak, was attributed to neutral Ba by a few further tests. A large  $\text{Ba}^+$  deposit is compared to a deposit made with the Ba getter in Fig. 5.3(a). The 619-nm and 670-nm peaks were observed with both sources, and since the getter produces only neutral Ba, they were attributed to neutralized ions in  $\text{Ba}^+$  deposits. Observation of the fluorescence with two different types of Ba sources is itself positive. In addition, observation of the fluorescence with the low deposit energy of the getter may bode well for the prospect of grabbing on a probe in LXe. Observation of a large deposit of  $\text{Ar}^+$  in SXe is also shown in Fig. 5.3(a). The lack of fluorescence further disfavors a matrix-damage-related source of the fluorescence, such as color centers. Finally, to rule out the possibility that the signal in Ba imaging experiments is due to passed wavelengths far from the 620-nm band-pass region, e.g. infrared, imaging experiments of  $\text{Ar}^+$  deposits in SXe

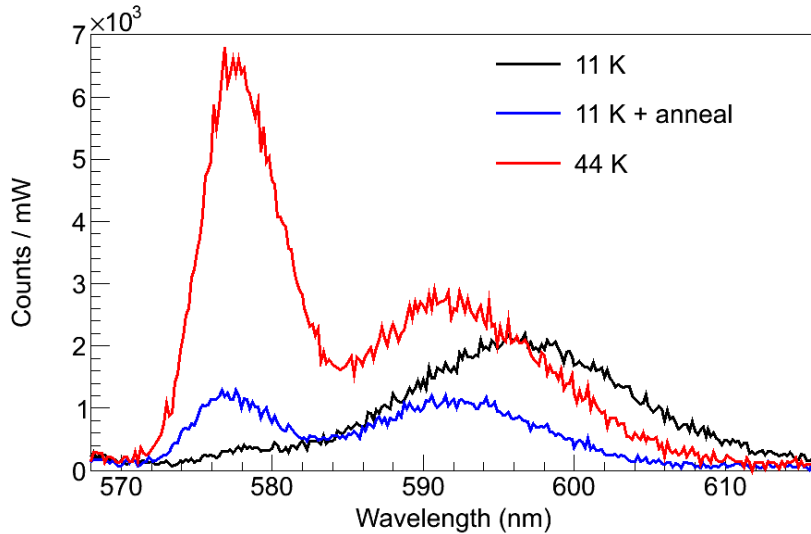


FIGURE 5.4. Spectra of peaks around 590 nm of a  $\text{Ba}^+$  deposit made at 11 K before and after annealing to 39.4 K, and one made at 44 K. All observations are at 11 K. Both  $\text{Ba}^+$  deposits are 15 s, however the 44 K deposit is scaled slightly to account for different ion current. Laser power was about 0.1 mW with an unfocused beam waist of  $w = 7.056$  mm, at 566 nm wavelength.

were performed with both pulsing and continuous ion beams. The same 620-nm band-pass filter was used, as well as the same focused 570-nm laser, to be similar to  $\text{Ba}^+$  619-nm imaging experiments. Summed counts from these deposits were consistent with background, as shown in Fig. 5.3(b).

### 5.3. ANNEALING/TEMPERATURE DEPENDENCE

Emission spectra can depend on annealing history, and similarly on the temperature at which a deposit is made. Spectra under different temperature conditions are shown in Fig. 5.4. Peak shapes look similar for deposits made at 40-55 K to those made at 11 K and then annealed to 40-55 K, where both are observed at 11 K. Differences in relative amplitudes could be due to differences in matrix site populations. The broader emission around 596 nm in non-annealed 11-K deposits is interpreted as a higher population of the 601-nm peak, as it is not resolved from the 591-nm peak. Deposit temperature dependence of the 619-nm peak

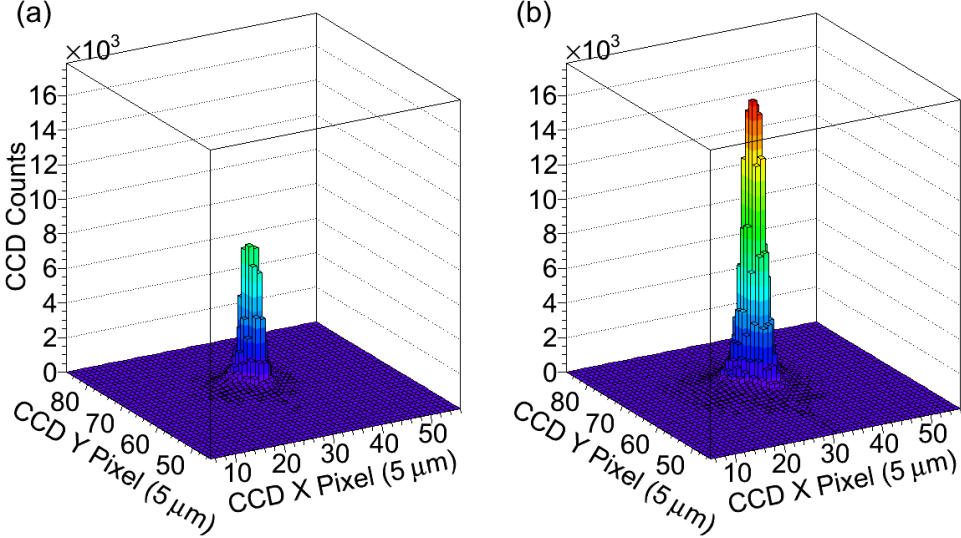


FIGURE 5.5. Images of 619-nm fluorescence in focused 570-nm laser region for deposits made at (a) 11 K and (b) 52 K. Deposits are 3 s of continuous  $\text{Ba}^+$  current. Exposures are 0.1 s at 11 K.

was studied by imaging the fluorescence from a focused laser through the 620-nm band-pass filter, shown in Fig. 5.5. The level of 619-nm signal is about  $3\times$  larger in deposits made at 52 K vs. 11 K. Imaging is described in detail in Chapter 6. These tests guided the standard of depositing at  $50\pm 5$  K when observing the 577-, 591-, and/or 619-nm peaks.

Fluorescence spectra with 564 nm excitation through several annealing cycles for a deposit made at 11 K are shown in Fig. 5.6. At this wavelength, all observed Ba peaks are prominent except the 570-nm peak. Initial exposure shows significant 591- and 601-nm (unresolved from one another) emission, with some 577-nm emission. All peaks are reduced at the high temperature ends of the anneal cycles, and return to lower temperatures shows recovery to an overall increase for some peaks, and overall loss of others. Fit peak counts (fitting is described in Sec. 4.2) vs. temperature are shown in Fig. 5.7. The 577-nm and 619-nm peaks gained significantly with the first anneal, suggesting that they are due to more stable matrix sites. Both of these peaks remained about the same after the second cycle (small gain

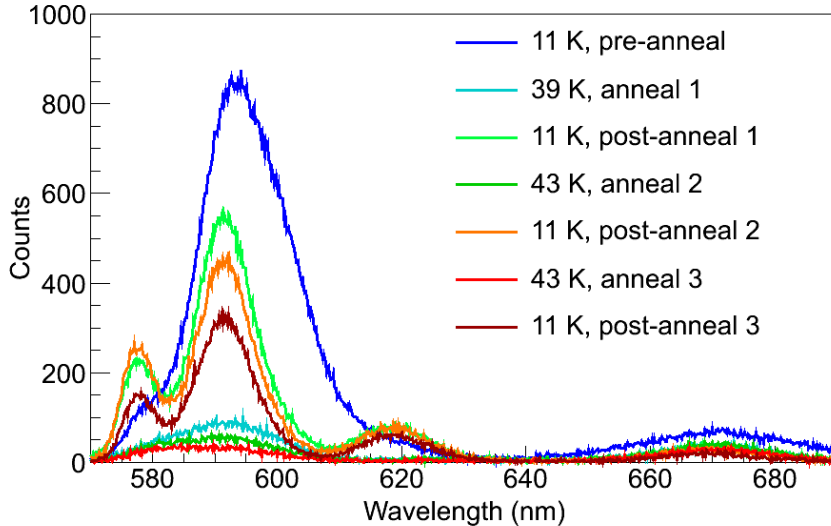


FIGURE 5.6. Spectra of a large  $\text{Ba}^+$  deposit through several annealing cycles. Initial deposit was at 11 K. Laser power was about 0.2 mW with an unfocused beam waist of  $w = 7.056$  mm, at 564 nm wavelength. These are selections from the full data set shown as peak counts vs. temperature in Fig. 5.7. [19]

in 577-nm), and both had loss after the third cycle, which reached the higher temperature of 48 K. The 591-nm had moderate loss with each cycle. The 601-nm peak had nearly complete loss in the first anneal cycle. The 670-nm peak had significant loss, with more loss after each succeeding anneal cycle, each of which reached higher a temperature than the last.

Aside from matrix site changes, direct temperature dependence of fluorescence can be observed in annealing cycles. The 577-, 591- and 619-nm peaks have their highest amplitude at 11 K. The 577-nm and 619-nm peaks reach a plateau at 11 K, while the 591-nm may benefit from even lower temperatures. The inverse relationship between fluorescence of these major peaks and temperature suggests that a probe in nEXO will need to be moved to an evacuated chamber in order to cool to 11 K or below for observation.

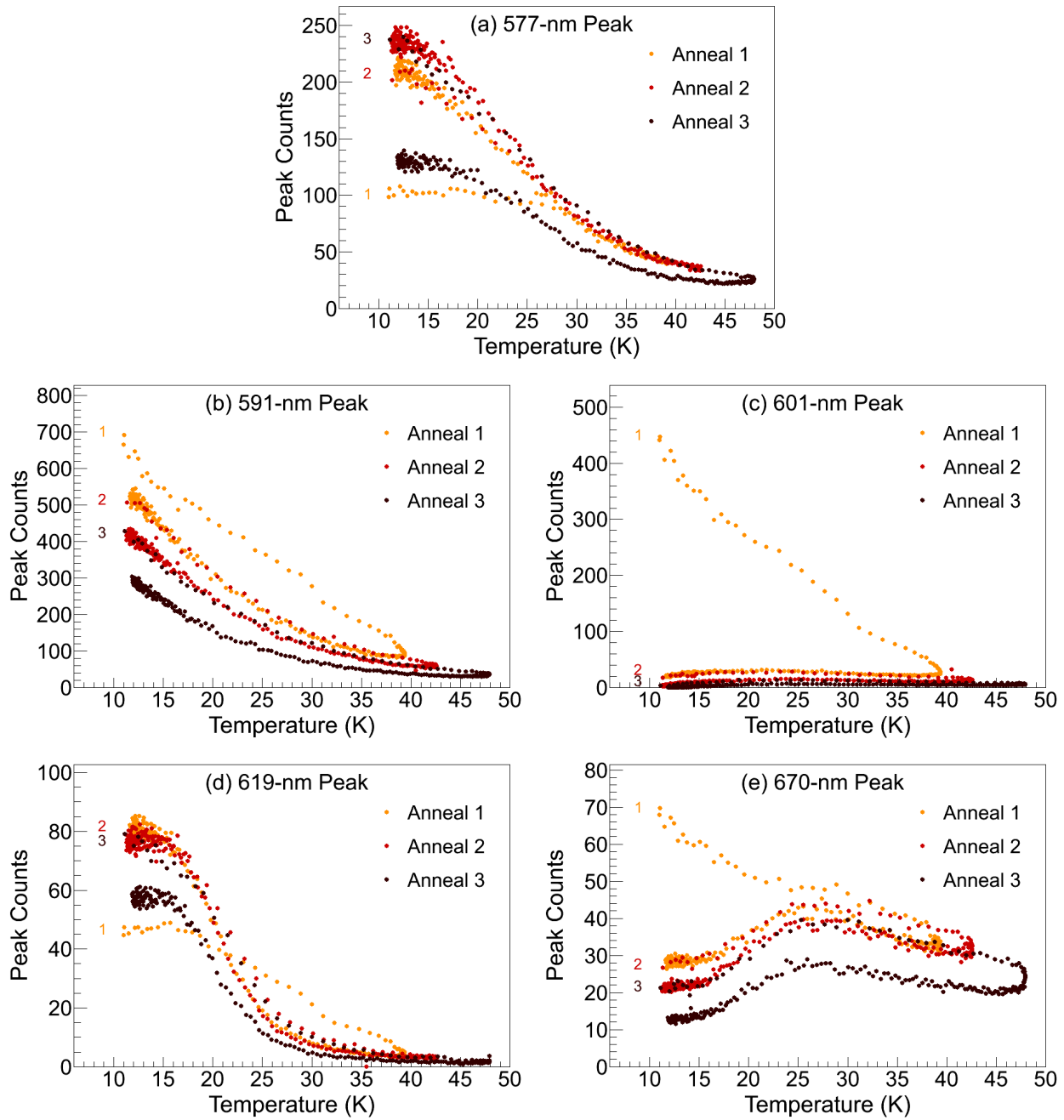


FIGURE 5.7. Fit peak counts for the (a) 577-, (b) 591-, (c) 601-, (d) 619-, and (e) 670-nm fluorescence peaks through three annealing cycles of the  $\text{Ba}^+$  deposit made at 11 K. “1”, “2”, and “3” mark the beginning of each anneal cycle. Laser power was about 0.2 mW with an unfocused beam waist of  $w = 7.056$  mm, at 564 nm wavelength.

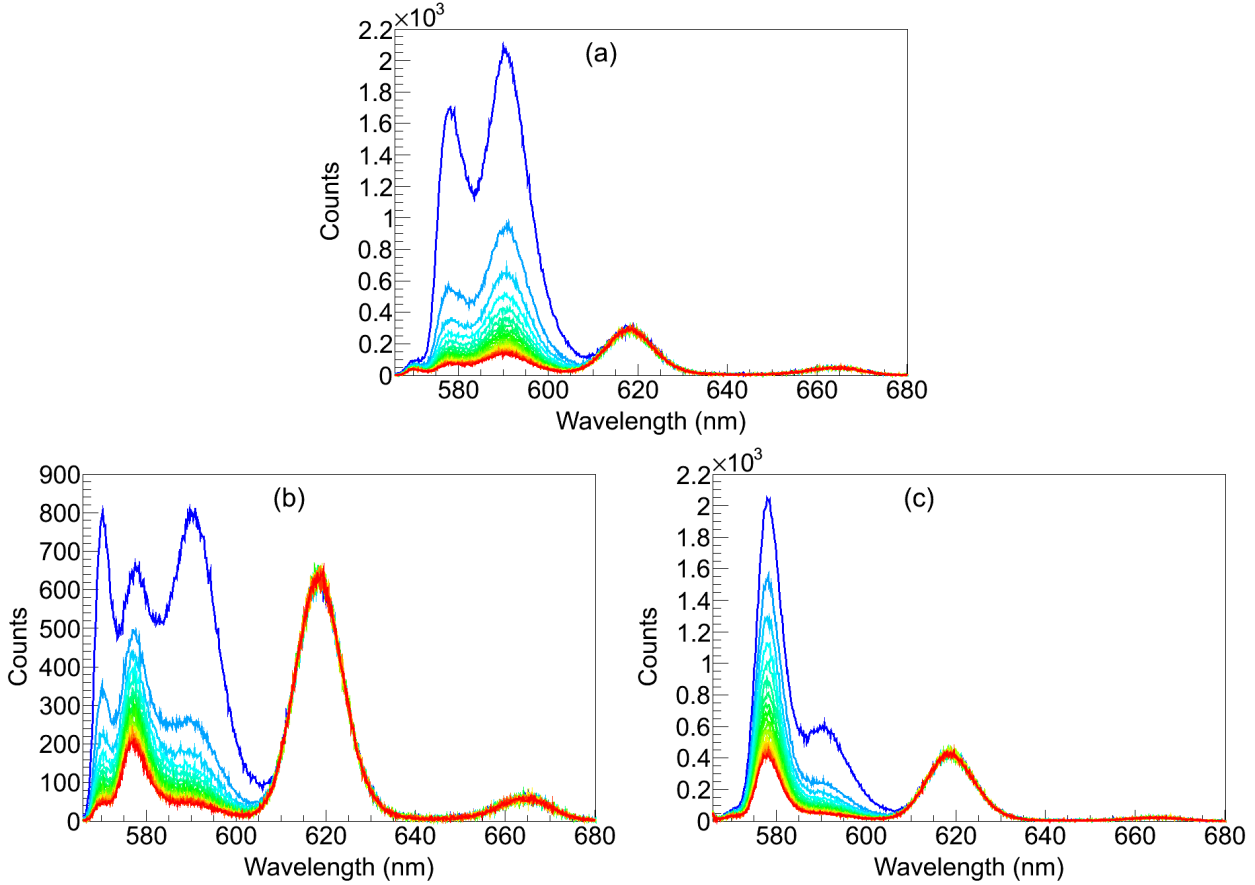


FIGURE 5.8. Bleaching Ba emission peaks with excitation at (a) 556.9 nm, (b) 562.6 nm, and (c) 566.3 nm. Laser power and exposure times are (a) 1.3 mW and 1 s, (b) 7.5 mW and 0.2 s, and (c) 5.8 mW and 0.2 s. Every tenth exposure is shown, beginning with the second in the darkest blue, ending with the darkest red. Each is a 5-s continuous  $\text{Ba}^+$  deposit at 45 K, observed at 11 K. [19]

#### 5.4. BLEACHING

Decay of fluorescence with laser exposure, or bleaching, was observed for all six Ba fluorescence peaks. Examples of bleaching spectra are shown in Fig. 5.8, with excitation at (a) 556.9 nm, (b) 562.6 nm, and (c) 566.3 nm, using a semi-focused laser of waist  $w = 1000 \mu\text{m}$ . Each curve is the Ba emission spectrum at different points in time. Bleaching was rapid for the 570-, 577-, 591-, and 601-nm peaks, and much slower for the 619- and 670-nm peaks.

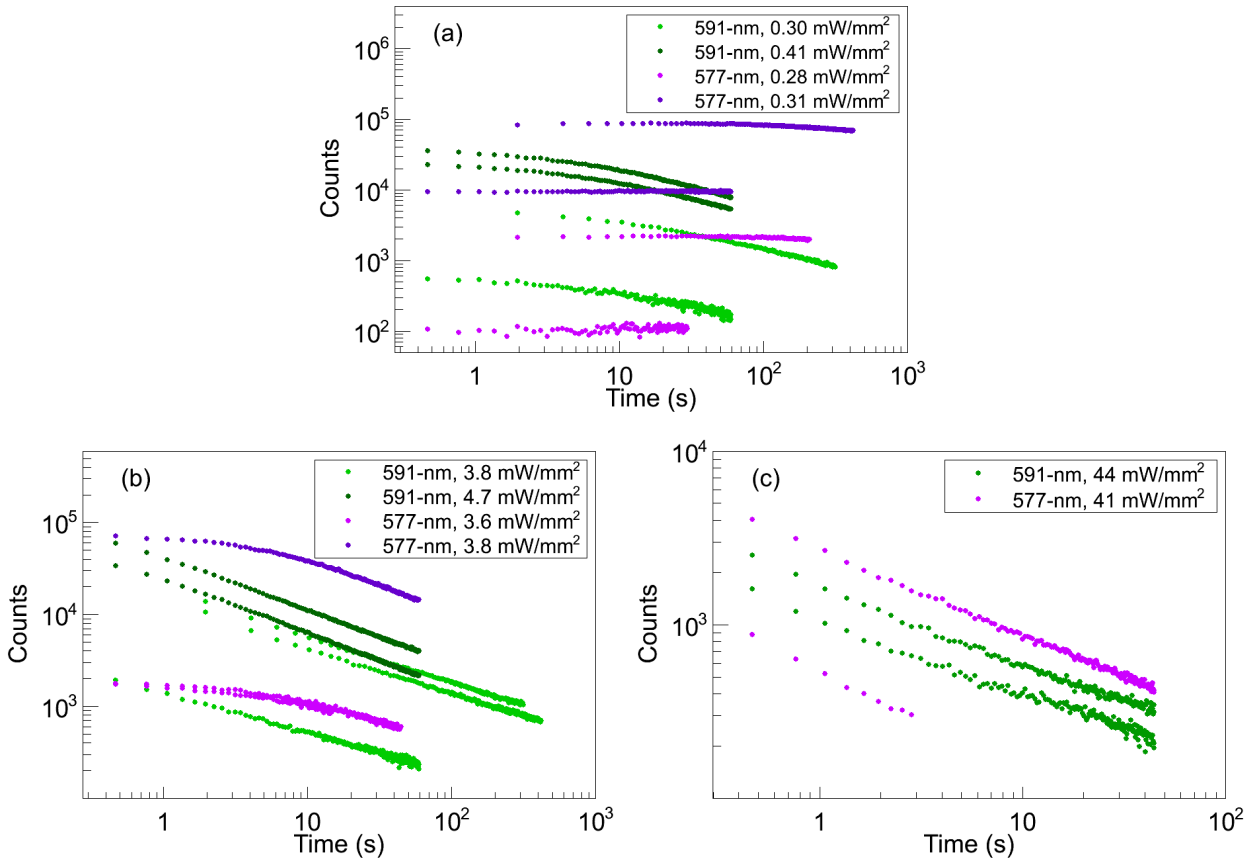


FIGURE 5.9. Fluorescence vs. time for three orders of magnitude (a,b,c) in laser intensity, for the 577-nm (purple) and 591-nm (green) fluorescence peaks. Deposits are continuous  $\text{Ba}^+$  at 45 K, observed at 11 K. Exposures are 0.2 or 2 s (indicated by point spacing minus 98.18 ms readout time).

#### 5.4.1. BLEACHING OF THE 577- AND 591-NM PEAKS

Fit integral fluorescence counts vs. time are shown in Fig. 5.9 for both the 577-nm (purple) and 591-nm (green) fluorescence peaks, with laser intensities on the order of (a) 0.33, (b) 4.0, and (c) 43  $\text{mW}/\text{mm}^2$ . Exact intensities are listed in the legends. The excitation wavelengths used for these comparisons were chosen to be optimal for the respective fluorescence peak: 566.3 nm was used for the 577-nm peak, and 562.6 nm for the 591-nm peak (see Fig. 5.2 for excitation spectrum). Bleaching was more rapid in the 591-nm peak when low intensity is used (a). For medium intensity (b), bleaching was more rapid for the 591-nm

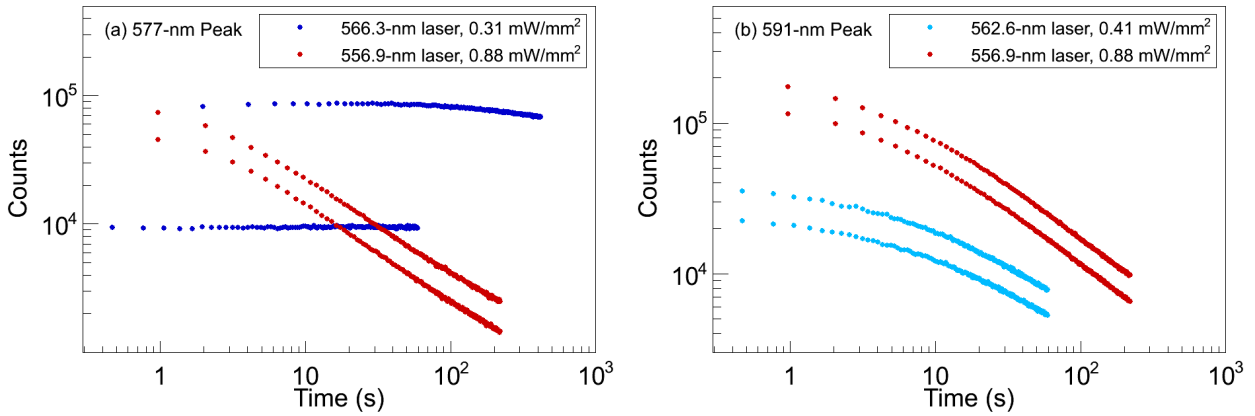


FIGURE 5.10. Fluorescence vs. time with different excitation wavelengths for (a) the 477-nm peak, and (b) the 591-nm peak. Deposits are continuous  $\text{Ba}^+$  at 45 K, observed at 11 K.

peak in the first 10 s, and then began approaching a similar rate to the 577-nm peak. For the high intensity (c), the rates began similar, with the 577-nm peak bleaching rate barely surpassing that of the 591-nm peak after about 20 s.

Comparisons of bleaching with different excitation wavelengths are shown in Fig. 5.10 for (a) the 577-nm peak, and (b) the 591-nm peak. In the case of the 577-nm peak (a), the excitation wavelengths (566.3 and 556.9 nm) correspond to different peaks in the excitation spectrum (Fig. 5.2). Very different bleaching rates were observed (although the 556.9-nm excitation had about  $2.5\times$  the intensity). In the case of the 591-nm peak (b), the excitation wavelengths (562.6 and 556.9 nm) correspond to neighboring peaks in the triplet structure of the excitation spectrum. The bleaching rates are similar, with a somewhat faster rate for the 556.9-nm excitation, which had about  $2\times$  the intensity.

Ultimately, these studies suggested the usage of the 577-nm peak in imaging small numbers of atoms due to its lower bleaching rate, especially with excitation on the high-wavelength end of the range studied. Imaging of Ba atoms using a combination of the 577-

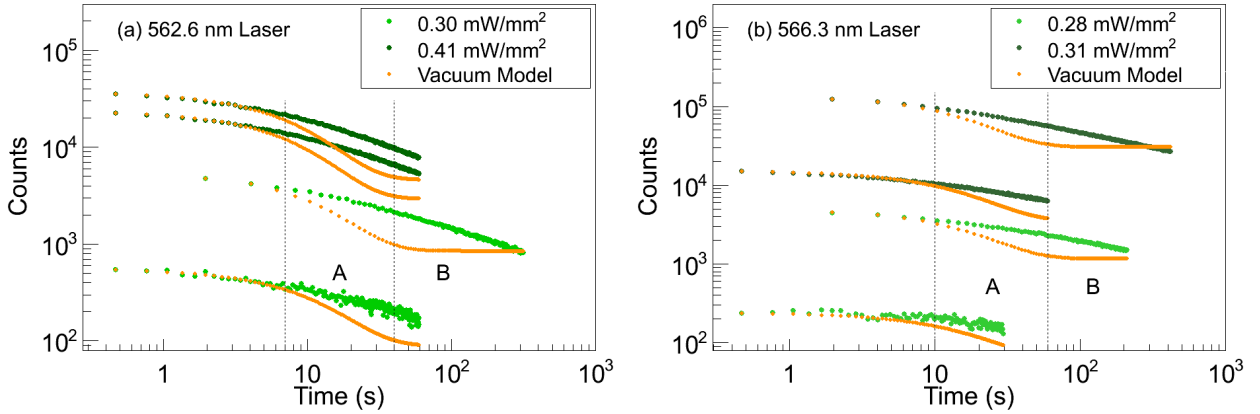


FIGURE 5.11. Vacuum model (orange) comparisons to bleaching data with excitation at (a) 562.6 nm, and (b) 566.3 nm. Regions A and B indicate behavioral differences. Deposits are continuous  $\text{Ba}^+$  at 45 K, observed at 11 K.

and 591-nm peaks with excitation at 566 nm, via a band-pass filter passing 573 - 599 nm FWHM, is discussed in Sec. 6.1.

A numerical model of fluorescence vs. time for a 5-level system of Ba in vacuum, described in Sec. 2.2 and using the Ba vacuum transition parameters given in Table 2.1, is compared to bleaching data of the 591-nm peak in Fig. 5.11 for excitation at (a) 562.6 nm, and (b) 566.3 nm. In the model, the input value for the excitation rate  $W_{12}$  is similar to the calculated value based on the laser power, laser radius, and cross-section of Ba in SXe of  $1.2 \times 10^{-15} \text{ cm}^2$  measured in [31], with slight adjustments.  $W_{12}$  is scaled by 0.8 for 562.6-nm excitation (a), and 0.5 for 566.3-nm excitation, which is explained by the lower value in the 591-nm peak excitation spectrum at 566.3 nm. Each model is normalized to the beginning of its respective data set. Agreement between the model and data is observed for the first several seconds of the bleaching process, and then deviation occurs in two major regions, A and B. In region A, the model predicts more rapid bleaching than is observed. In region B, the model predicts a leveling off as a steady state in energy level populations is reached, though the data continues to decay beyond this region.

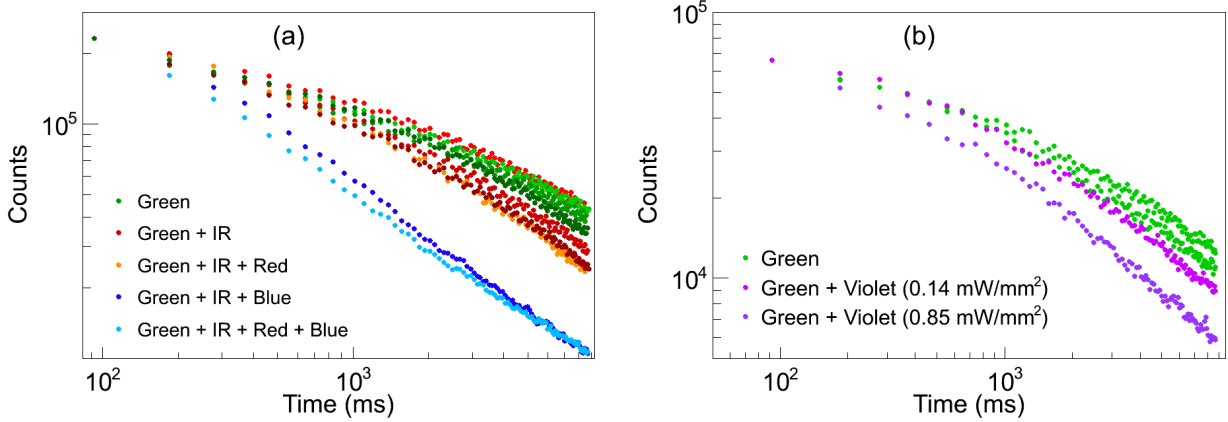


FIGURE 5.12. Bleaching data with and without additional re-pump lasers at (a) 1064 nm ( $\sim 18$  mW/mm $^2$ ), 1550 nm ( $\sim 9$  mW/mm $^2$ ), 657 nm ( $\sim 9$  mW/mm $^2$ ) and 472.64 nm ( $\sim 14$  mW/mm $^2$ ), and (b) 406 nm. All curves have 1.4 - 1.5 mW of 555-nm excitation, semi-focused to around 600-\$\mu\text{m}\$ beam waist. Deposits are (a) 6 s and (b) 3 s continuous Ba $^+$  at 11 K.

#### 5.4.2. RE-PUMPING

Re-pumping of optically pumped Ba could require up to three additional lasers, one for each of the populated metastable D states. The optimal excitation wavelength for each transition would need to be discovered using tunable lasers in the infrared. However, mixing of states and/or alterations in transition rates for Ba in the Xe matrix could lower the number of lasers needed. Re-pumping was attempted, with low-cost and on-hand lasers, for the direct infrared transitions as well as the higher-level transitions shown in Fig. 2.1. A 1550-nm diode laser and a 1064-nm Nd:YAG laser were used to attempt direct re-pumping from the  ${}^1\text{D}$  and  ${}^3\text{D}$  states, respectively. A 657-nm diode laser was used to attempt excitation from the  ${}^3\text{D}$  states into the higher-level  $5d6p\ {}^3\text{D}_1{}^\circ$  state, similar to the red laser utilized in the Ba MOT in [24] for the  $6d5d\ {}^3\text{D}_1$  state. The blue C480 dye laser and 406-nm Kr ion laser were used to attempt excitation from the  ${}^1\text{D}$  state into the higher-level states  $6s7p\ {}^1\text{P}_1{}^\circ$  and  $6s8p\ {}^1\text{P}_1{}^\circ$ , respectively.

591-nm fluorescence counts vs. time for several  $\text{Ba}^+$  deposits made and observed at 11 K are shown in Fig. 5.12 for several laser combinations, all of which were combined by dichroic filters into the same path. Each curve is a separate deposit, all of which are scaled to begin at the same point for comparison. In Fig. 5.12(a), green-only (555 nm) excitation (i.e., no re-pump lasers) is shown along with green + IR (1064 nm and 1550 nm), green + IR + red (657 nm), green + IR + blue (C480 dye at 472.64 nm), and green + IR + red + blue. Increased bleaching was observed by inclusion of these re-pump lasers, especially with the blue laser. In Fig. 5.12(b), green-only is shown again along with green + violet (Kr ion laser at 406 nm) at two different powers. Increased bleaching was observed with the violet laser, with more bleaching at the higher violet laser power.

#### 5.4.3. BLEACHING OF THE 619-NM PEAK

The 619-nm peak does bleach somewhat at much higher laser intensities. At a few mW of 570-nm excitation, bleaching is observed when the laser is focused. Integrated 619-nm fluorescence, divided by laser power, vs. time from an image of a focused 570-nm laser is shown in Fig. 5.13. Three scalings of laser power and exposure time were used such that  $I \times t$  is conserved, e.g. the curve with 0.21 mW laser power (green) has 1/3 the exposure time of that with 0.07 mW (blue). The deviation from linearity in the higher-power curves demonstrates more bleaching per excitation. Since  $I \times t$  is conserved, this indicates a time-dependent return mechanism for the fluorescence which is less helpful on shorter time scales. Shorter exposure times are more convenient, however this must be balanced against a loss of signal-to-noise. The 0.21 mW laser power was chosen for imaging experiments, described in Sec. 6.2.

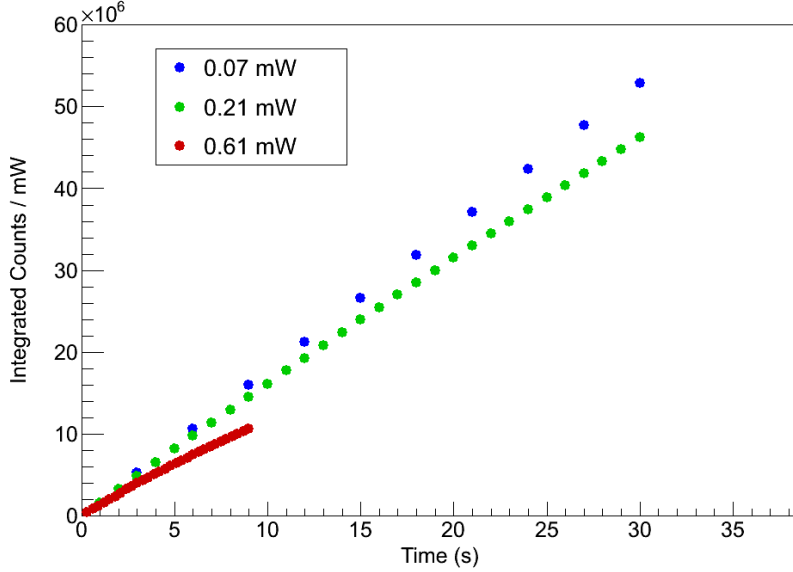


FIGURE 5.13. Integrated 619-nm fluorescence counts/mW for three laser powers, with exposure time scaled to conserve  $I \times t$ . Excitation is 570 nm focused to  $w_x \times w_y$  beam waists of  $2.06 \mu\text{m} \times 2.66 \mu\text{m}$ . All one deposit of 5 s continuous  $\text{Ba}^+$  at 50 K, observed at 11 K from low to high laser intensity.

### 5.5. FLUORESCENCE EFFICIENCY OF 577- AND 591-NM PEAKS

The fluorescence efficiency ( $\epsilon_f$ ), defined in Sec. 2.4, was measured by the total counts observed near the beginning of exposure, before substantial bleaching has occurred.  $\epsilon_f$  vs. excitation rate ( $W_{12}$ ) is shown in Fig. 5.14 for the 577- and 591-nm peaks, where  $W_{12}$  is calculated using the cross-section of Ba in SXe measured in [31] of  $1.2 \times 10^{-15} \text{ cm}^2$ .  $\epsilon_f$  is fairly constant below  $W_{12} \approx 100 \text{ s}^{-1}$ , and begins to decline at higher  $W_{12}$ . This is explained by higher effect of bleaching at higher  $W_{12}$  in the first exposure. Using the lowest values of  $W_{12}$ ,  $\epsilon_f$  is measured to be about  $2 \times 10^{-3}$  for the 591-nm peak with 562.6-nm excitation, and  $5 \times 10^{-4}$  for the 577-nm peak with 566.3-nm excitation.

### 5.6. BLUE EXCITATION / CANDIDATE $\text{BA}^+$ LINES

Blue excitation of  $\text{Ba}^+$  in SXe was first explored in the thesis of Shon Cook, wherein a set of sharp emission peaks were observed at 522, 575, 637, 712, and 814 nm, in decreasing

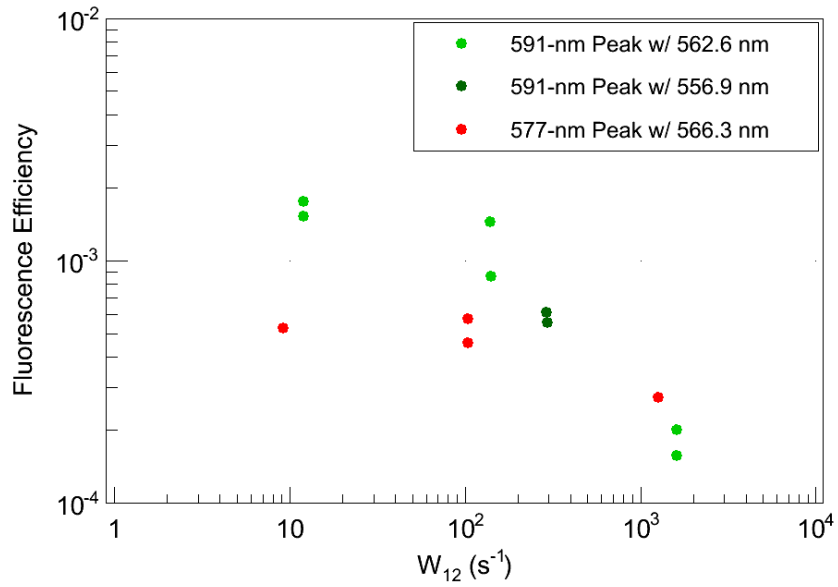


FIGURE 5.14. Fluorescence efficiency vs.  $W_{12}$  using the first exposure frame for the 577-nm (red) and 591-nm (green) peaks. Deposits are 5 s continuous  $\text{Ba}^+$  at 50 K, observed at 11 K with laser radius  $w = 1000 \mu\text{m}$ .

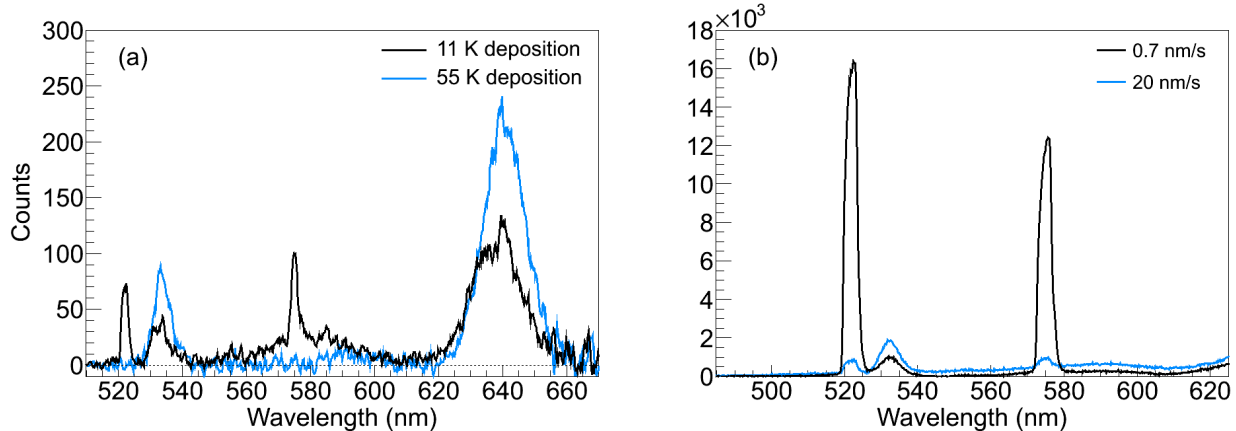


FIGURE 5.15. Comparison of  $\text{Ba}^+$  deposits made at (a) 55 K vs. 11 K, and (b) 20 nm/s vs. 0.7 nm/s.[19]

amplitude. These peaks were attributed to emission from different vibrational states of a molecule composed of Ba and one or more H atoms [30]. This attribution was supported by two additional experiments. Firstly, a reduction of those peaks is observed in deposits made at 50 K, well above the  $\text{H}_2$  freezing temperature of 12 K, vs. deposits made at 11 K, as shown in Fig. 5.15(a). Secondly, the peaks are much stronger in deposits made with lower

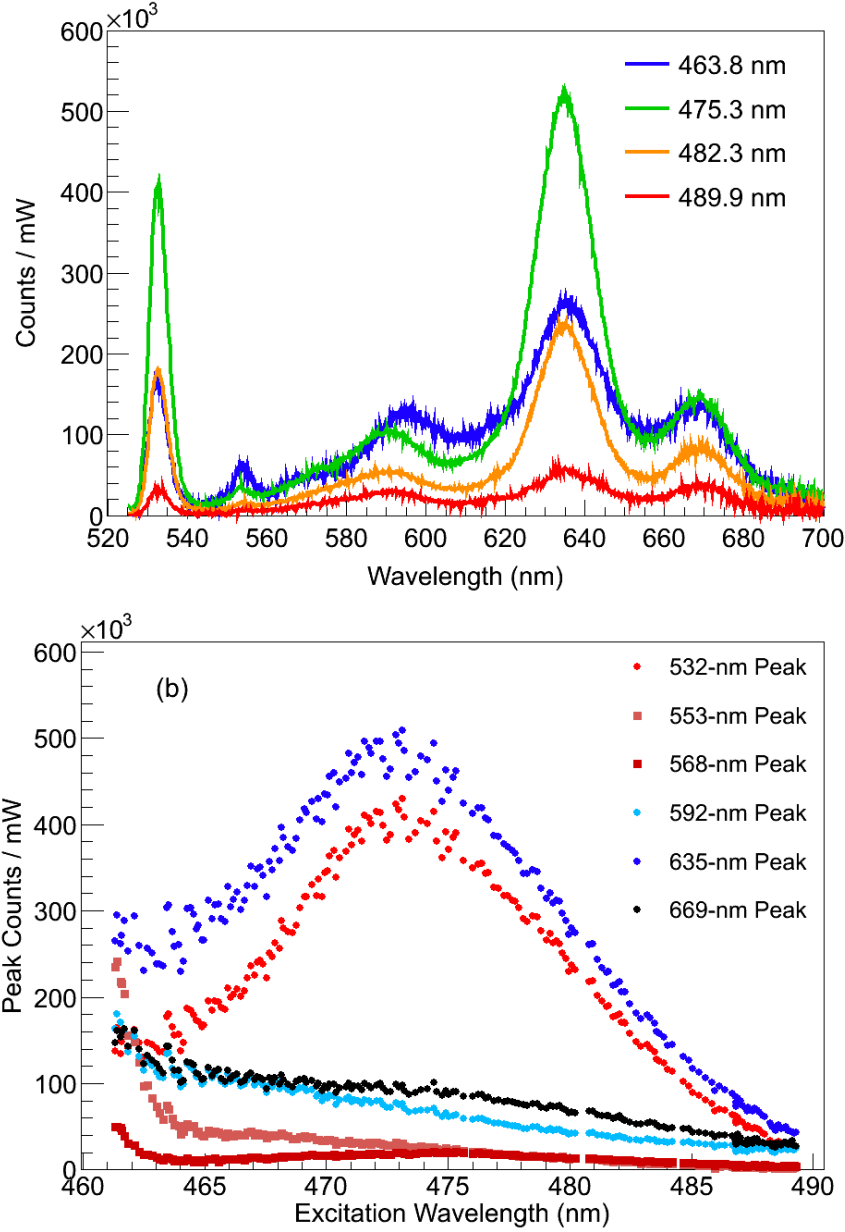


FIGURE 5.16. (a) Background-subtracted fluorescence spectra for a few different excitation wavelengths, and (b) excitation spectra for peaks observed through C480 dye range.

leak rates, as shown in Fig. 5.15(b), for deposits made at 11 K. This is explained by a higher concentration of H<sub>2</sub> impurities in a matrix formed with a lower leak rate.

In contrast to lower BaH<sub>x</sub> emission, several other emission peaks become prominent in deposits made at 50±5 K and observed at 11 K. Representative spectra at a few excitation

wavelengths are shown in 5.16(a). An excitation spectrum, shown in 5.16(b), was produced for each emission peak, similar to spectra with green excitation, by scanning the C480 dye laser and fitting the spectrum in each frame. Fitting is described in Sec, 4.2.2. Of particular interest are the peaks at 532 nm and 635 nm. These peaks have identical excitation spectra, indicating that they are due to the same excitation transition. Thus the 532- and 635-nm peaks may be due to relaxation to the ground and metastable D states, respectively, from one of the excited P states of Ba<sup>+</sup> in SXe. However, matrix effects would need to be responsible for the higher number of counts observed in the 635nm peak vs. the 532-nm peak, whereas the P → S transition is about 4× more likely than the P → D transition in vacuum. The resemblance between the excitation spectra for the 592- and 669-nm peaks, as well as between the 553- and 568-nm peaks, is also interesting.

## CHAPTER 6

### RESULTS: IMAGING

Results presented in Chapter 5 determined the ideal conditions for imaging small numbers of Ba atoms in SXe. Ideal excitation wavelengths were determined by studying the excitation spectra of the signal as well as the background. Bleaching of the fluorescence determined ideal laser intensities to be used. Studies of deposits made and observed at different temperatures determined the procedure of depositing at  $50 \pm 5$  K and observing at 11 K. Imaging of the 577- and 591-nm fluorescence is presented in 6.1 down to  $\leq 2.7 \times 10^3$  average atoms exposed, and imaging of the 619-nm peak is presented down to the single-atom level in Sec 6.2. Initial scanned images of  $\text{Ba}^+$  deposits are presented in 6.3.

Though the imaging spectrometer can produce spacial images with the 0-order grating reflection, better collection efficiency and imaging quality are achieved by removing the spectrometer and imaging directly onto the CCD. Band-pass filters were used to pass the desired Ba fluorescence peak(s) while attenuating laser scatter and sapphire fluorescence.

An example image of the focused 570 nm dye laser on a  $\text{Ba}^+$  deposit is shown in Fig. 6.1. With  $4\times$  magnification, each pixel is  $5 \mu\text{m} \times 5 \mu\text{m}$ . The laser's path through the window is faintly visible by the tail of the broad  $\text{Cr}^{3+}$  fluorescence in the 620-nm band-pass filter. The laser is focused at the top surface of the window, which faces the ion beam. The surface background is seen on the back surface, and the 619-nm Ba fluorescence stands out above both backgrounds on the top surface. The observed size of the laser spot, with a  $1/e^2$  radius of about  $12 \mu\text{m}$ , is larger than the  $2.06 \mu\text{m} \times 2.66 \mu\text{m}$   $1/e^2$  laser spot size. Aberrations and vibrations in the collection optics could contribute to this, as well as cryostat vibrations.

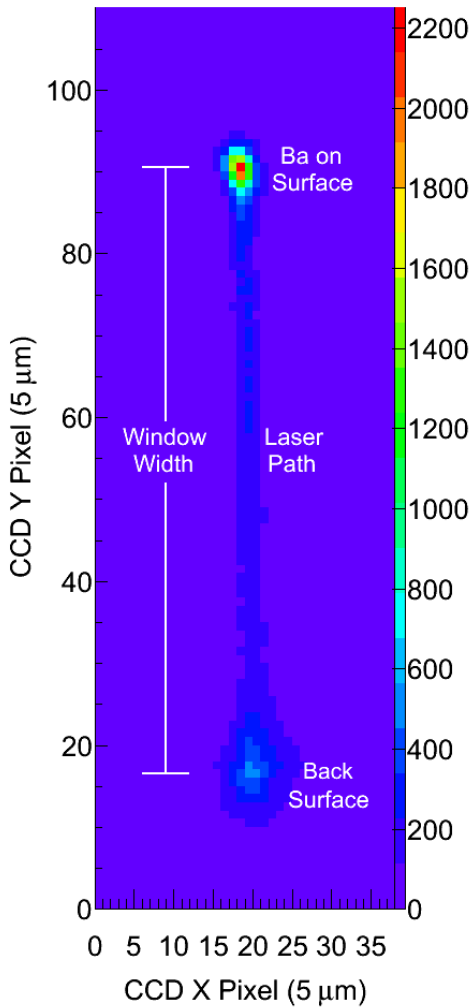


FIGURE 6.1. Example image of focused laser exciting a  $\text{Ba}^+$  deposit on a c-plane sapphire window of 0.5 mm thickness. A 620-nm band-pass filter passes the fluorescence.

### 6.1. IMAGING 577- AND 591-NM PEAKS

First attempts at imaging small numbers of Ba atoms in a focused laser region were done with the 577- and 591-nm Ba fluorescence peaks together using a 586-nm band-pass filter, which passes 573 - 599 nm FWHM. This filter has a 2" diameter, resulting in a factor of  $4 \times$  more collection efficiency. An image of  $\leq 2.7 \times 10^3$  atoms on average, with  $\leq 8.3 \times 10^3$  total atoms exposed, is shown in Fig. 6.2 for a 100-s exposure with 0.02  $\mu\text{W}$  of 566-nm excitation.

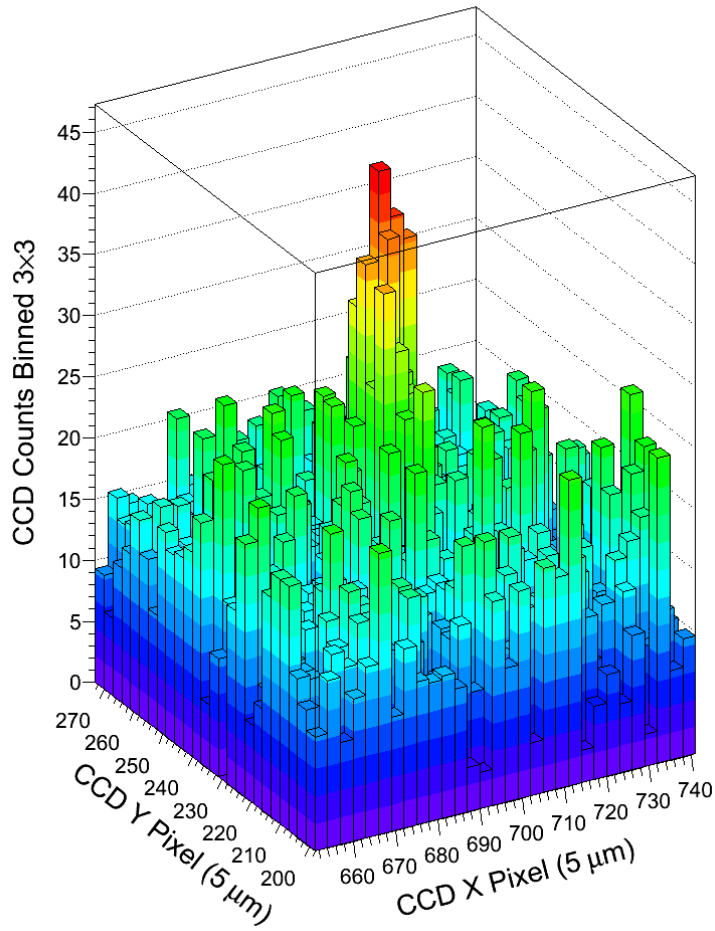


FIGURE 6.2. Image of  $\leq 2.7 \times 10^3$  average Ba atoms in SXe. 100-s exposure with  $.02 \mu\text{W}$  of 566 nm excitation, deposited at 50 K and observed at 11 K.  $3 \times 3$  CCD pixel binning.

The distinction between average and total is described in Sec. 3.6. At this low intensity, no bleaching was observed in the four frames observed (frame 1 is shown). Groups of 9 ( $3 \times 3$ ) CCD pixels are binned to produce the nice peak shown. As discussed in 5.4, detection of very small numbers of atoms in these sites may require several re-pump lasers. As a result of low total exposure, neither the sapphire nor the surface backgrounds are present in these images, though a Xe-only image has been subtracted.

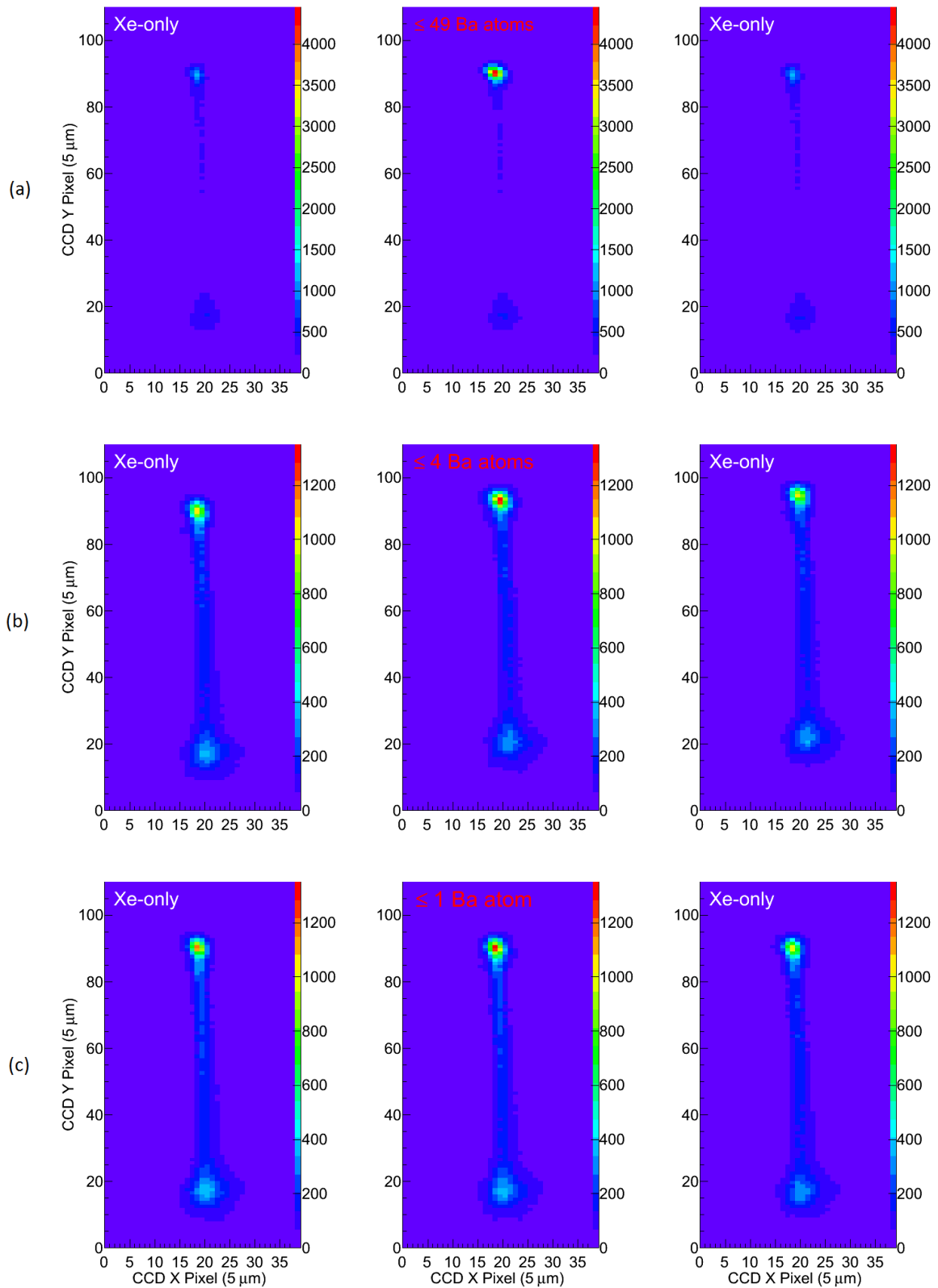


FIGURE 6.3. Raw images of three  $\text{Ba}^+$  deposits yielding (a)  $\leq 49$ , (b)  $\leq 4$ , and (c)  $\leq 1$  average  $\text{Ba}$  atoms, with their preceding and succeeding  $\text{Xe}$ -only deposits.

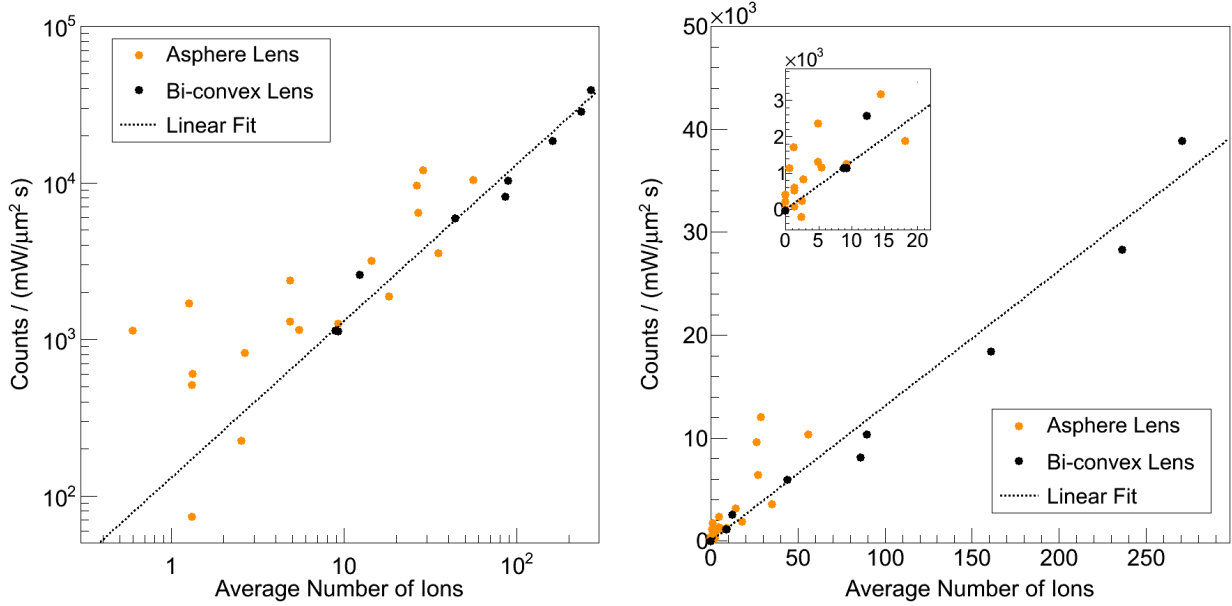


FIGURE 6.4. 619-nm signal, scaled by laser intensity and exposure time, vs. average number of  $\text{Ba}^+$  exposed by focused laser at 570 nm for experiments with two different laser focusing lenses.

## 6.2. IMAGING 619-NM PEAK

Raw images of  $\text{Ba}^+$  deposits and their preceding and succeeding Xe-only deposits are shown in Fig. 6.3 for deposits of (a)  $\leq 49$  ( $\leq 230$ ), (b)  $\leq 4$  ( $\leq 20$ ), and (c)  $\leq 1$  ( $\leq 5$ ) average (total) Ba atoms. Signal is distinguishable from background by eye, even at the 1-atom average signal level. The lack of historical buildup of Ba fluorescence between deposits, even for large  $\text{Ba}^+$  deposits, is important for the implementation of this method of Ba tagging on a probe in nEXO.

619-nm fluorescence signal is plotted vs. average ions (upper limit on atoms) exposed in Fig. 6.4, on log and linear scales, for many deposits in two experiments with two different laser focusing lenses. The bi-convex laser-focusing lens with no astigmatism compensation (black) resulted in a larger laser region and a lower intensity than the aspherical lens with astigmatism compensation (orange). Signal was determined by summing the counts of a 3-pixel  $\times$  3-pixel ( $15\mu\text{m} \times 15\mu\text{m}$ ) region centered on the laser spot in the image, and background

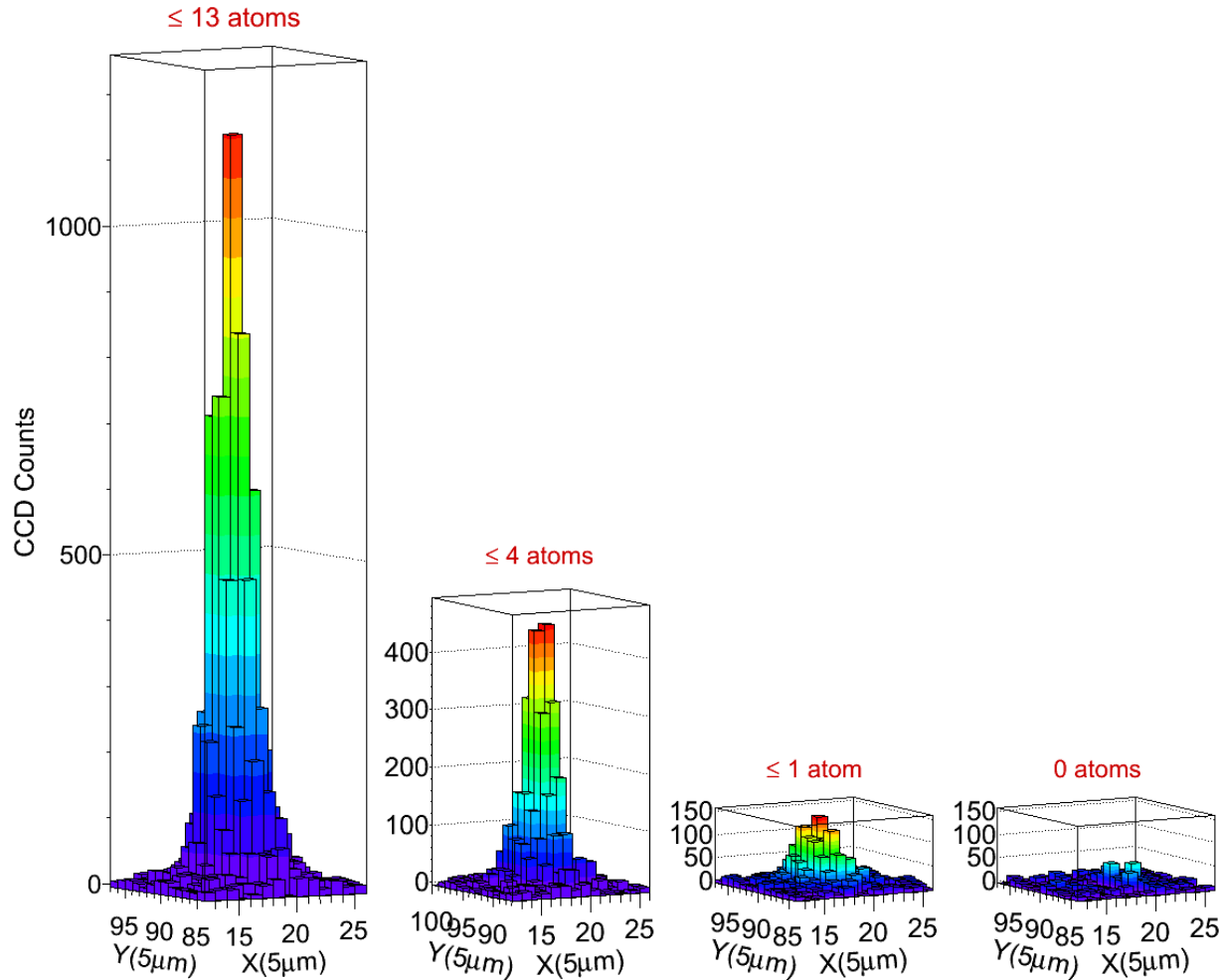


FIGURE 6.5. Subtracted images of 619-nm fluorescence in focused laser region for runs near linear trend line in signal vs. ions deposited. Exposure is 60 s with 570 nm excitation.

was determined by averaging the 3-pixel×3-pixel sum of the Xe-only runs before and after each Ba<sup>+</sup> run. Signal and background were scaled to laser intensity and exposure time respective to each experiment, with laser power respective to each individual run, and then background was subtracted. The two experiments demonstrate a linear relationship between signal and number of ions exposed over nearly three orders of magnitude. The linear scale includes a zoom into small numbers of ions in the inset. Zero ion deposits are produced by retracting the Faraday cup for 1 s without pulsing the ion beam. The slope of the linear fit,

which does not include a constant value, gives about  $131 \pm 6$  counts/atom, where counts are scaled by laser intensity ( $\text{mW}/\mu\text{m}^2$ ) and exposure time (s). Deposits at the single-ion level average to about  $800 \pm 240$  counts. Subtracted images of 619-nm Ba fluorescence are shown in Fig. 6.5 for a few deposits near the linear trend line.

### 6.3. SCANNED IMAGES

The ultimate demonstration of single-atom imaging will be to scan the focused laser over samples of separated Ba atoms, observing a peak when the laser moves over individual atoms. Preliminary scans were performed by scanning the focusing lens in a grid pattern, using the setup described in Sec. 3.7. Summed counts from the focused laser region, scaled by laser intensity and exposure time, are plotted vs. grid position for several deposits in Fig. 6.6. These scans are grids of 20 points in X at about  $3.75 \mu\text{m}/\text{step}$ , by 5 points in Y at about  $4.78 \mu\text{m}/\text{step}$ . An overall higher signal is observed with 48.4 average  $\text{Ba}^+/\text{step}$  (c), however single-atom peaks are not distinguished in the sparse deposit of 0.18 average  $\text{Ba}^+/\text{step}$  (b). The aspherical laser focusing lens and astigmatism compensator are used for  $w_x \times w_y = 2.06 \mu\text{m} \times 2.66 \mu\text{m}$   $1/e^2$  laser region, though cryostat vibrations increase the exposed region as described in Sec. 3.6. This had the effect of exposing neighboring step regions to the laser. Similar to the procedure in single-location imaging experiments, pre-bleaching of the surface background was done with a scan of the dye laser at 580.5 nm, in a  $22 \times 7$  grid centered on the  $20 \times 5$  grid used during the following experiment, with 10 s at each location.

Scans from the data set in Fig. 6.6 reveal step-to-step variation in the background, which is dominated by the surface background. The difference in counts between successive grid steps is shown as a distribution in Fig.6.7 for all Xe-only deposits in this set of deposits.

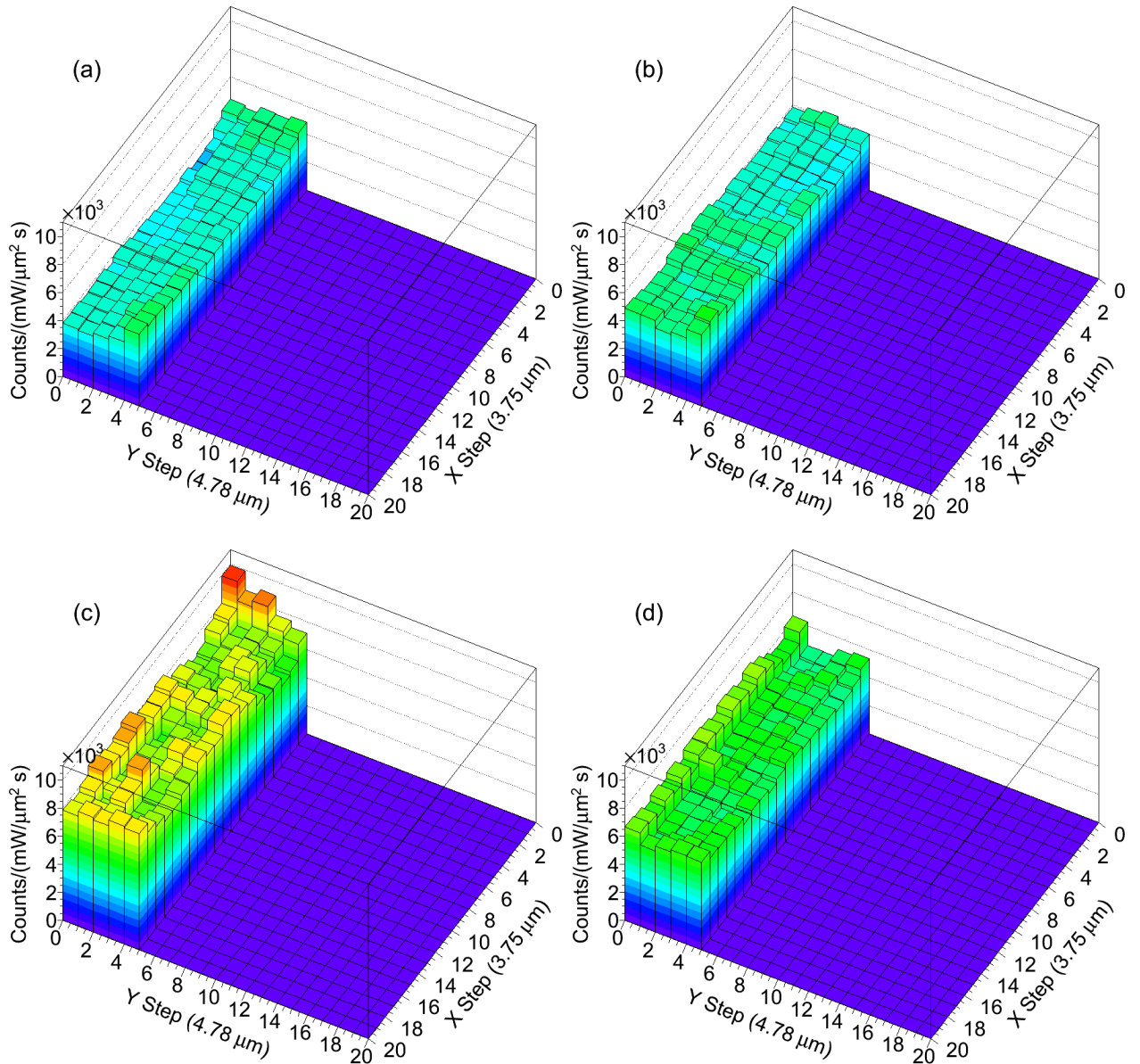


FIGURE 6.6. Early attempts at scanned images of a few deposits: (a) Xe-only, (b) 0.18 average  $\text{Ba}^+$ /step, (c) 48.4 average  $\text{Ba}^+$ /step, and (d) Xe-only. 10-s exposures with 0.4–0.5 mW of focused 570 nm laser.

Fluctuations occurred at the level of the  $800 \pm 240$  counts single-atom signal, and above the level of the  $131 \pm 6$  trend line single-atom signal. Single-atom signals are not expected to stand out under these conditions. Average counts per step, again scaled by laser intensity and exposure time, are plotted vs. average number of ions per step in Fig. 6.8, overlain in

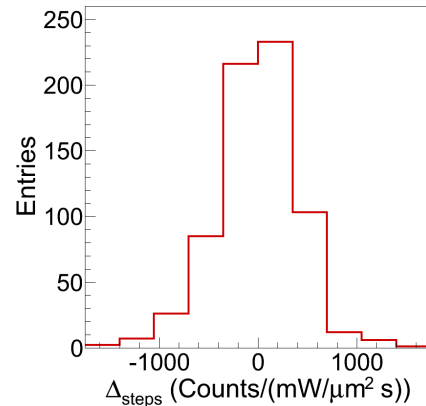


FIGURE 6.7. Distribution of difference in counts ( $\Delta_{\text{steps}}$ ) between successive scan frames in Xe-only deposits.

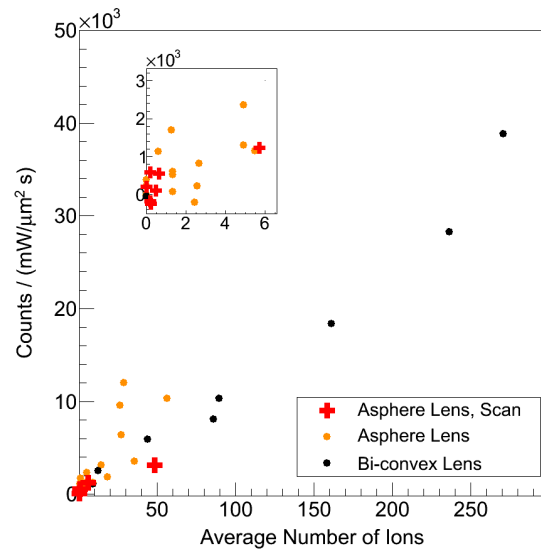


FIGURE 6.8. 619-nm signal, scaled by laser intensity and exposure time, vs. average number of  $\text{Ba}^+$  exposed by focused laser at 570 nm from Fig. 6.4 with that of scanned images of  $\text{Ba}^+$  deposits.

blue crosses on the data from Fig. 6.4, demonstrating signal levels consistent with previous experiments. Next steps in scanned imaging are discussed in Sec. 7.1.

## CHAPTER 7

# CONCLUSIONS

The achievement of single-atom-level imaging of Ba atoms in SXe is significant progress toward the ability to tag barium daughters in the nEXO LXe TPC. Improved studies of the spectroscopy of Ba in SXe have been presented and utilized in reaching this level of sensitivity with the 619-nm fluorescence, as well as in imaging the 577- and 591-nm fluorescence for deposits down to  $\leq$  around  $10^3$  atoms. Blue excitation of  $\text{Ba}^+$  deposits in SXe has revealed several newly reported emission peaks which are candidates for matrix-isolated  $\text{Ba}^+$  ions.

### 7.1. FUTURE WORK

The next major demonstration will be imaging separate Ba atoms in SXe in scanned images. As indicated in Sec. 6.3, overcoming the challenge of variable surface background emission is the first priority. Studies of fluorescence lifetimes of the 619-nm signal vs. the background using a pulsed laser and a photo-multiplier tube for fast detection will be explored, in order to determine whether a photon-sorting technique may remove background. The atom counting inherent in scanned images will provide the first measurement of the percentage of deposited  $\text{Ba}^+$  ions visible via the 619-nm fluorescence.

Exploration of re-pumping wavelengths for the 577- and 591-nm peaks, as well as the 570- and 601-nm peaks, will be done using tunable lasers in the infrared. The ability to count atoms emitting with these different wavelengths would be very valuable. It is not yet known how deposits made by freezing on a probe in LXe will look. The ability to count ions will be pursued by continuing study of the candidate  $\text{Ba}^+$  emission peaks with blue excitation.

Ultimate demonstrations of Ba tagging in SXe will be done by grabbing out of LXe on cold probes. Construction of an apparatus is occurring simultaneously in Fairbank's laboratory by Adam Craycraft, in which a cold probe can be lowered into a LXe cell. Ba<sup>+</sup> will be produced by laser ablation of Ba metal and drifted into the LXe and onto the cold probe by electrodes. In order to reach temperatures around 10 K, where the Ba fluorescence is strong, the probe will be raised to an isolated pumping region for further cooling and observation.

## BIBLIOGRAPHY

- [1] C.D. Ellis and W.A. Wooster, “The average energy of disintegration of radium e,” *Proceedings of the Royal Society (London)* **A117** 109-123 (1927).
- [2] F. Wilson, *American Journal of Physics* **36**, 12 (1968).
- [3] Y. Fukuda *et al.* (Super-Kamiokande Collaboration), *Phys. Rev. Lett.* **81** 1562 (1998).
- [4] S.T. Petcov, W. Rodejohann, T. Shindou, Y. Takanishi, *Nuclear Physics B* **739**, 208233 (2006).
- [5] M. Danilov *et al.*, *Physics Letters B* **480**, 1218 (2000).
- [6] K.A. Olive *et al.* (Particle Data Group), “14. Neutrino Mass, Mixing, and Oscillations,” *Chin. Phys. C* **38**, 090001 (2014) (<http://pdg.lbl.gov>)
- [7] P.A.R. Ade *et al.* (Planck Collaboration), *Astronomy and Astrophys.* **571**, A16 (2014).
- [8] N. Steinbrink *et al.*, *New Journal of Physics* **15**, 113020 (2013).
- [9] J. Albert *et al.* (EXO-200 Collaboration), *Phys. Rev. C* **89**, 015502 (2014).
- [10] M. Moe, *Phys. Rev. C* **44**, R931 (1991).
- [11] M. Auger *et al.*, *JINST* **7**, P05010 (2012).
- [12] R. Nielson *et al.*, *Nuclear Instruments and Methods in Physics Research A* **608**, 68 (2009).
- [13] E. Conti *et al.*, *Phys. Rev. B* **68**, 054201 (2003).
- [14] J. Albert *et al.* (EXO-200 Collaboration), *Nature* **510**, 229 (2014).
- [15] N. Ackerman *et al.* (EXO-200 Collaboration), *Phys. Rev. Lett.* **107**, 212501 (2011).
- [16] A. Gando *et al.* (KamLAND-Zen Collaboration), *Phys. Rev. C* **86**, 021601 (2012).
- [17] K. Hall, *In-situ Laser Tagging of Barium Ions in Liquid Xenon for the EXO Experiment*. Colorado State Universtiy Thesis/Dissertation (2012).
- [18] K. Twelker *et al.*, *Review of Scientific Instruments* **85**, 095114 (2014).

- [19] B. Mong *et al.*, *Phys. Rev. A* **91**, 022505 (2015).
- [20] T. Brunner *et al.*, *International Journal of Mass Spectrometry* **379**, 110-120 (2015).
- [21] J. J. Curry, *Journal of Physical and Chemical Reference Data* **33**, 725 (2004).
- [22] A. Mohanty *et al.*, *Hyperfine Interactions* **233**, 113-119 (2015).
- [23] N. Yu, W. Nagourney, H. Dehmelt, *Phys. Rev. Lett.* **78**, 26 (1997).
- [24] S. De, U. Dammalapati, K. Jungmann, L. Willmann, *Phys. Rev. A* **79**, 041402(R) (2009).
- [25] M. Green *et al.*, *Phys. Rev. A* **76**, 023404 (2007).
- [26] E. Whittle, D. Dows, G. Pimentel, *The Journal of Chemical Physics* **22**, 1943 (1954).
- [27] C. Crepin-Gilbert and A. Tramer, *Int. Reviews in Physical Chemistry* **18**, No. 4, 485-556 (1999).
- [28] L. C. Balling and J. J. Wright, *The Journal of Chemical Physics* **83**, 5 (1985).
- [29] L. W  hlin, "The Colutron, a Zero Deflection Isotope Separator," *Nuclear Instruments and Methods* **27** 55-60 (1964).
- [30] S. Cook, *Detection of Small Numbers of Barium Ions Implanted in Solid Xenon for the EXO Experiment*. Colorado State Universtiy Thesis/Dissertation (2012).
- [31] B. Mong, *Barium Tagging in Solid Xenon for the EXO Experiment*. Colorado State Universtiy Thesis/Dissertation (2011).
- [32] A. C. Sinnock, *J. Phys. C: Solid St. Phys.* **13**, 2375-91 (1980).
- [33] Tache, J.-P., *Applied Optics* **26**, 429 (1987).
- [34] D. F. Nelson, M. D. Sturge, *Physical Review* **137**, 4A (1965).
- [35] C. Guguschev, J. Gotze, M. Gobbels, *American Mineralogist* **95**, 449-455 (2010).
- [36] R. A. Ford, O. F. Hill, *Spectrochimica Acta* **16**, 493-496 (1960).

- [37] D. S. McClure, *Solid State Phys.* **9**, 399-525 (1959).
- [38] D. Richard Sears, Harold P. Klug, *The Journal of Chemical Physics* **37**, 12 (1962).